

Spectroscopy of CASSOWARY gravitationally-lensed galaxies in SDSS: characterisation of an extremely bright reionization-era analog at $z = 1.42$

Ramesh Mainali^{1,2,3}★, Daniel P. Stark², Tucker Jones⁴†, Richard S. Ellis⁵, Yashar D. Hezaveh^{6,7}, & Jane R. Rigby¹

¹ *Observational Cosmology Lab, NASA Goddard Space Flight Center, Greenbelt, MD 20771, USA*

² *Steward Observatory, University of Arizona, 933 N Cherry Ave, Tucson, AZ, USA*

³ *Department of Physics, The Catholic University of America, Washington, DC 20064, USA*

⁴ *Department of Physics, University of California Davis, 1 Shields Avenue, Davis, CA 95616, USA*

⁵ *Department of Physics and Astronomy, University College London, Gower Street, London, WC1E 6BT, UK*

⁶ *Center for Computational Astrophysics, Flatiron Institute, 162 Fifth Avenue, New York, NY 10010, USA*

⁷ *Département de Physique, Université de Montréal, Montreal, Quebec, Canada H3T 1J4*

Accepted XXX. Received YYY; in original form ZZZ

ABSTRACT

We present new observations of sixteen bright ($r = 19 - 21$) gravitationally lensed galaxies at $z \simeq 1 - 3$ selected from the CASSOWARY survey. Included in our sample is the $z = 1.42$ galaxy CSWA-141, one of the brightest known reionization-era analogs at high redshift ($g=20.5$), with a large sSFR (31.2 Gyr^{-1}) and an $[\text{OIII}]+\text{H}\beta$ equivalent width ($\text{EW}_{[\text{OIII}]+\text{H}\beta}=730 \text{ \AA}$) that is nearly identical to the average value expected at $z \simeq 7 - 8$. In this paper, we investigate the rest-frame UV nebular line emission in our sample with the goal of understanding the factors that regulate strong $\text{CIII}]$ emission. Whereas most of the sources in our sample show weak UV line emission, we find elevated $\text{CIII}]$ in the spectrum of CSWA-141 ($\text{EW}_{\text{CIII}]}=4.6 \pm 1.9 \text{ \AA}$) together with detections of other prominent emission lines ($\text{OIII}], \text{Si III}], \text{Fe II}^*, \text{Mg II}$). We compare the rest-optical line properties of high redshift galaxies with strong and weak $\text{CIII}]$ emission, and find that systems with the strongest UV line emission tend to have young stellar populations and nebular gas that is moderately metal-poor and highly ionized, consistent with trends seen at low and high redshift. The brightness of CSWA-141 enables detailed investigation of the extreme emission line galaxies which become common at $z > 6$. We find that gas traced by the $\text{CIII}]$ doublet likely probes higher densities than that traced by $[\text{OII}]$ and $[\text{SII}]$. Characterisation of the spectrally resolved Mg II emission line and several low ionization absorption lines suggests neutral gas around the young stars is likely optically thin, potentially facilitating the escape of ionizing radiation.

Key words: galaxies: evolution - galaxies: formation - galaxies: high-redshift

1 INTRODUCTION

Over the last decade, much progress has been made in our understanding of galaxies in the first billion years of cosmic time (for a review, see Stark 2016). Deep infrared imaging has uncovered thousands of photometrically-selected star forming systems thought to lie in the redshift range $6 < z < 9$ (e.g., McLure et al. 2013; Finkelstein et al. 2014; Bouwens et al. 2015, 2021; Livermore et al. 2017; Ishigaki et al. 2018), providing a census of UV-selected galaxies throughout the reionization era. The spectral energy distributions (SEDs) point toward a population undergoing rapid stellar mass

growth with blue UV continuum spectral slopes (e.g., Rogers et al. 2013; Bouwens et al. 2014), low stellar masses and large specific star formation rates (Stark et al. 2013b; González et al. 2014; Grazian et al. 2015; Salmon et al. 2015; Curtis-Lake et al. 2016).

In the last five years, our first constraints on the nebular emission properties of galaxies at these early epochs have emerged. *Spitzer*/IRAC photometry suggests that nearly half of the UV-selected galaxies at $z \simeq 7$ have extremely large $[\text{OIII}]+\text{H}\beta$ equivalent widths (EWs) (Labbé et al. 2013; Smit et al. 2014, 2015; Roberts-Borsani et al. 2015; De Barros et al. 2017; Endsley et al. 2020), indicating that very recent ($\lesssim 50$ Myr) activity powers the UV and optical luminosity, as expected for galaxies undergoing rapidly rising star formation histories. Roughly 20% of the popula-

★ E-mail: ramesh.mainali@nasa.gov

tion have yet more intense rest-optical nebular emission ($[\text{OIII}]+\text{H}\beta$ $\text{EW} > 1000 \text{ \AA}$), indicating an extremely young stellar population ($< 10 \text{ Myr}$) is dominating the light, as expected for systems that have undergone a recent burst of star formation. Since such extreme emission line galaxies (EELGs) are very rare at lower redshifts (Boylett et al. 2022), we lack a detailed understanding of the gas and ionizing agents in typical reionization-era systems.

Ground-based near-infrared spectrographs offer a path toward progress at the highest redshifts, providing access to the rest-frame ultraviolet where a suite of valuable diagnostic lines are situated. The first deep spectra have revealed strong nebular emission from high ionization metal species ($[\text{CIII}], \text{CIII}] \lambda\lambda 1907, 1909 \text{ \AA}$, $[\text{OIII}] \lambda\lambda 1660, 1666 \text{ \AA}$, $\text{CIV} \lambda\lambda 1548, 1550 \text{ \AA}$), a significant departure from what is commonly seen at lower redshifts (Stark et al. 2015b,a, 2017; Mainali et al. 2017; Laporte et al. 2017; Mainali et al. 2018; Hutchison et al. 2019; Topping et al. 2021). The detection of these lines reveals gas under extreme ionization conditions and points to a population of intense ionizing agents, potentially AGN in some cases (Laporte et al. 2017; Mainali et al. 2018) and low metallicity massive stars in others (Mainali et al. 2017; Stark et al. 2017; Berg et al. 2019, 2021). The detection of $\text{CIV} \lambda\lambda 1548, 1550 \text{ \AA}$ and $[\text{CIII}], \text{CIII}] \lambda\lambda 1907, 1909 \text{ \AA}$ may further indicate a higher fraction of ionizing photons escape from a galaxy (Schaerer et al. 2022). While the equivalent width distribution in the total population is still subject to limited statistics (Mainali et al. 2018), it appears that both the gas and ionizing sources at $z \gtrsim 6$ are often significantly different from that in galaxies at $z \simeq 2 - 3$.

The presence of strong rest-UV nebular emission in a subset of $z \gtrsim 6$ galaxies bodes well for future studies of the reionization era. For the next-generation 25-30m ground based optical/infrared observatories (which are limited to constraints on the rest-frame UV at $z > 6$), these lines may provide the only way in which early galaxies can be studied spectroscopically. While typically fainter than the strong lines in the rest-optical, the suite of emission lines in the far-UV provide unique diagnostic power of the ionizing spectrum and gas physical conditions (i.e., density, temperature, ionization). Meanwhile in the near-UV, the resonant nature of the nebular Mg II emission line makes it an ideal probe of the neutral gas opacity in early galaxies, potentially providing an indirect indicator of LyC leakage at $z \gtrsim 6$ (e.g., Henry et al. 2018; Chisholm et al. 2020; Xu et al. 2022; Izotov et al. 2022; Seive et al. 2022). The advantage of Mg II relative to Ly α is that it is not obscured by the neutral IGM at very high redshifts.

To ensure that the faint rest-UV spectra provide reliable physical diagnostics from these future facilities, it is important that we understand the gas conditions and stellar populations which support prominent UV line emission. With current facilities, this is most easily done at lower redshifts where rest-frame optical emission lines which constrain the gas-phase metallicity and ionization parameter are observable with ground-based facilities. Over the last few years, a wide range of observations have been conducted with the goal of better understanding the physics regulating rest-UV emission line spectra. These studies have demonstrated that prominent CIII] appears to be a fairly ubiquitous feature in the rest-UV spectra of dwarf star forming galaxies (Erb et al. 2010; Christensen et al. 2012; Stark et al. 2014; Rigby et al. 2015; Vanzella et al. 2016, 2017; Senchyna et al. 2017; Berg et al. 2018; Mainali et al. 2020; Du et al. 2020; Schmidt et al. 2021; Tang et al. 2021; Llerena et al. 2021; Berg et al. 2022; Mainali et al. 2022), reflecting the large electron temperatures associated with metal poor gas and the hard ionizing spectrum of young, low metallicity massive stars.

Here we seek to build on this progress, improving our un-

derstanding of the connection between UV line emission and the physical properties of the massive stars and ionized gas. Over the last decade, we have utilized a wide range of ground-based facilities (LBT, Keck, Magellan) to obtain deep spectra and imaging of some of the brightest known ($g=19-21$) $z \simeq 1.5 - 3$ gravitationally lensed galaxies within Sloan Digital Sky Survey (SDSS). This sample contains galaxies with a range of physical properties, including two of the brightest known systems with the large specific star formation rates (and extreme emission lines) that are typical in the reionization era. Central to this observational campaign are newly-acquired optical spectra from the Echellette Spectrograph and Imager (ESI; Sheinis et al. 2002) on the Keck II telescope (see Jones et al. 2018 for more details). The ESI spectra provide moderate resolution ($R=6300$) rest-UV spectra, enabling a unique exploration of the nature of the massive stars and the physical conditions of the ionized gas. We supplement the Keck observations (9 galaxies) with optical spectra from LBT (1 galaxy) and MMT (6 galaxies), near-infrared spectra from Magellan, and new optical and near-infrared imaging.

The large continuum brightness of the SDSS lensed galaxies offers several distinct advantages with respect to the much fainter low mass galaxies that are typical of cluster fields imaged by *HST* (e.g., Christensen et al. 2012; Stark et al. 2014; Vanzella et al. 2017). First, it enables improved constraints on the ionized gas physical conditions (metallicity, density, ionization parameter) through detection of the full suite of rest-optical strong emission lines as well as occasionally allowing detection of multiple temperature and density-sensitive lines, providing a more comprehensive view of the conditions in the gas and the most important factors regulating the rest-UV line spectra. Second, the large continuum S/N in the rest-UV spectra makes it possible to detect very weak rest-UV nebular lines. This enables the rest-UV lines to be characterized in individual galaxies for a wide range of gas conditions, not only in the most extreme and metal-poor systems. This will provide a valuable control sample for our analysis, offering insight into what factors are most important in regulating rest-UV emission line spectra. This insight will be critical in assessing the feasibility of detecting and characterizing lines in the rest-frame far and near-UV with future facilities. In this paper, we will focus primarily on CIII] emission, comparing measured line strengths to other empirical and model-based quantities (i.e., gas-phase metallicity, optical line ratios with the goal of understanding the factors regulating the CIII] strength.

The paper is organized as follows. We present the new imaging and spectra and discuss population synthesis modeling of broadband SEDs in §2. In §3, we provide our results on individual galaxies. We discuss implications of our spectra of a reionization-era analog in §4 and summarize our findings in §5.

Throughout the paper, we adopt a Λ -dominated, flat universe with $\Omega_\Lambda = 0.7$, $\Omega_M = 0.3$ and $H_0 = 70 \text{ km s}^{-1} \text{ Mpc}^{-1}$. All magnitudes in this paper are quoted in the AB system and equivalent widths (EW) are given in rest-frame, unless stated otherwise.

2 OBSERVATIONS AND ANALYSIS

2.1 Sample Selection

The galaxies studied in this paper were originally identified using a search algorithm that identifies blue arcs surrounding red early type galaxies in Sloan Digital Sky Survey (SDSS) imaging as part of the Cambridge And Sloan Survey Of Wide ARcs on the sky (CASSOWARY; e.g., Belokurov et al. 2007, 2009). The most recent catalog of CASSOWARY lensed galaxies was presented in Stark

Object	RA	DEC	z_{spec}	m_{AB}	Dates	Rest-UV Coverage (Å)	t_{exp} (ksec)	PA (deg)	M_{UV}	μ	Instrument
CSWA-165	01:05:19.65	+01:44:56.4	2.127	21.1	12 Dec 2012	1020-2560	3.6	5.0	-22.0	5.4 ^a	MMT/BCS
CSWA-116	01:43:50.13	+16:07:39.0	1.499	20.8	29 Sep 2011	1280-3200	2.7	105	-20.9	10.7 ^a	MMT/BCS
CSWA-103	01:45:04.18	-04:55:42.7	1.959	22.1	8-10 Nov 2012	1350-3425	25	115	-20.9	4.7 ^a	Keck/ESI
CSWA-164	02:32:49.97	-03:23:29.3	2.512	19.9	8-10 Nov 2012	1140-2880	28	158	-22.0	20.8 ^a	Keck/ESI
CSWA-11	08:00:12.37	+08:12:07.0	1.409	21.1	24 March 2012	1330-3280	1.8	60	-22.3	1.9 ^c	MMT/BCS
CSWA-139	08:07:31.51	+44:10:48.5	2.536	22.1	23 Mar 2012	905-2260	3.6	80	-20.8	3.8 ^a	MMT/BCS
CSWA-141	08:46:47.53	+04:46:09.3	1.425	20.5	8 Nov 2012	1655-4180	5.2	190	-22.1	5.5 ^a	Keck/ESI
...	11 Nov 2015	1440-2140	3.6	190	LBT/MODS
CSWA-19	09:00:02.64	+22:34:04.9	2.032	20.9	9-10 Nov 2012	1320-3330	20	86	-21.9	6.5 ^a	Keck/ESI
CSWA-40	09:52:40.22	+34:34:46.1	2.189	21.4	5-6 Mar 2013	1255-3175	16.2	70	-22.3	3.2 ^a	Keck/ESI
CSWA-2	10:38:43.58	+48:49:17.7	2.196	20.9	5 Mar 2013	1250-3125	7.2	17	-22.3	8.4 ^a	Keck/ESI
CSWA-16	11:11:03.68	+53:08:54.9	1.945	22.1	24 Mar 2012	1085-2715	2.7	267	-20.8	3.9 ^d	MMT/BCS
CSWA-38	12:26:51.69	+21:52:25.5	2.925	21.3	6 Mar 2013	1020-2580	10.8	130	-20.2	40 ^b	Keck/ESI
CSWA-13	12:37:36.20	+55:33:42.9	1.864	20.3	24 Mar 2012	1120-2790	1.8	320	-23.0	1.9 ^d	MMT/BCS
CSWA-39	15:27:45.02	+06:52:33.9	2.762	20.9	5-6 Mar 2013	1065-2695	18	105	-21.5	15 ^b	Keck/ESI
CSWA-128	19:58:35.65	+59:50:53.6	2.225	20.6	8-10 Nov 2012	1240-3140	16.3	60	-21.9	10 ^c	Keck/ESI
CSWA-163	21:58:43.68	+02:57:30.2	2.081	22.4	30 Sep 2011	1035-2600	1.8	20	-20.4	6.5 ^a	MMT/BCS

^aStark et al. (2013a), ^bKoester et al. (2010), ^cLeethochawalit et al. (2016), ^dThis work.

Table 1. Summary of rest-frame UV observations of our bright gravitationally lensed CASSOWARY galaxy sample. New ultra-deep moderate resolution optical spectra have been obtained for nine of these sources using ESI on Keck. We also include an additional seven sources from Stark et al. (2013a) with high quality MMT blue channel spectra. From left to right, we present the object ID in the CASSOWARY catalog, the RA and DEC, the spectroscopic redshift, apparent magnitude, the date the optical spectra were obtained, the rest-UV wavelength coverage provided by the optical spectra, the exposure time and position angle of the optical spectra, the absolute magnitude of the arc in the rest-UV, the magnification factor provided by gravitational lensing, and the optical spectrograph utilized. Further details are presented in §2.

et al. (2013a) following a large spectroscopic campaign aimed at obtaining redshifts of the source and lens galaxies. The catalog of galaxies released in Stark et al. (2013a) contains more than 50 gravitationally-lensed galaxies in SDSS. Optical magnitudes of this sample are in the range $19.6 < r < 22.3$.

Here we present the results from a large observational investment targeting sixteen of these bright lensed sources with Keck, Magellan, LBT, and MMT (see Table 1). Object identifiers from the CASSOWARY survey are abbreviated as “CSWA” in the table and subsequent discussion. A mosaic of the galaxies considered in this paper is shown in Figure 1. In the following subsections, we describe the imaging and spectral datasets that we have obtained for this paper. The galaxies considered here were selected from the larger sample of Stark et al. (2013a) based on the brightness of the continuum. We also preferentially targeted sources at redshifts which place rest-optical lines in regions of significant atmospheric transmission in the near-IR.

2.2 Spectroscopy

2.2.1 Optical Spectroscopy

We have acquired deep Keck/ESI optical spectra of nine galaxies from the Stark et al. (2013a) sample (see Table 1 for details), enabling robust constraints to be placed on the strength of nebular UV metal line emission. The positioning of the ESI slit on the lensed galaxies is shown in Figure 1. The spectra were obtained in two observing runs between November 2012 and March 2013. The ESI spectra cover observed wavelengths between 4000 to 10100 Å, providing rest-frame spectral coverage that typically ranges between 1300 and 2000 Å (see Table 1). A slit width of $0''.75$ was used, providing a resolving power of $R=6300$ ($FWHM=48 \text{ km s}^{-1}$). The data were reduced using the ESIRedux code written by J. X. Prochaska. Sky subtraction is performed following the bias subtraction and flat

fielding. The 1D spectra are then extracted using a boxcar aperture matched to the spatial extent of the arc. When multiple lensed images appear on the slit, the traces are extracted separately and then combined to maximize the S/N. The continuum is generally well detected, with $S/N \simeq 10$ per resolution element at 6200 Å. Example spectra are shown in Figure 2. A full description of the ESI observations and spectral reduction is presented in Jones et al. (2018).

One source in the ESI sample, CSWA-141, was also observed with the Multi Object Double Spectrograph (MODS, Pogge et al. 2010) on the LBT. MODS provides bluer wavelength coverage than ESI, allowing constraints to be placed on emission from CIV, OIII], and He II. We used a long slit of width $0''.8$ with the 400 lines/mm grating, providing spectral resolution of ~ 3 .

We also include seven other galaxies from Stark et al. (2013a) for which the MMT Blue Channel Spectrograph (BCS) discovery spectra have sufficient continuum S/N to characterize the rest-UV metal emission lines. The MMT BCS data were obtained with the 300 lines/mm grating, providing total spectral coverage of ~ 5300 . For the slit width of $1''.0$ used in the observations, the typical spectral resolution is ~ 6.5 . More details of the MMT observations are provided in Stark et al. (2013b).

In total, the Keck, LBT, and MMT data provides rest-UV spectra for 16 galaxies. Our aim is to characterize CIII] emission feature, typically the strongest rest-UV emission line, along with other rest-UV emission features in the whole sample. Using redshift presented in Jones et al. (2018) for Keck/ESI data and Stark et al. (2013a) for MMT data, we first searched for CIII] emission in individual galaxy spectrum. The line is spectrally resolved in the Keck spectra, whereas it remained unresolved in the MMT spectra. For the resolved CIII] doublet, we measured emission line fluxes and associated errors (for error spectrum) in individual components by directly integrating the flux levels within ± 1 Å of individual line

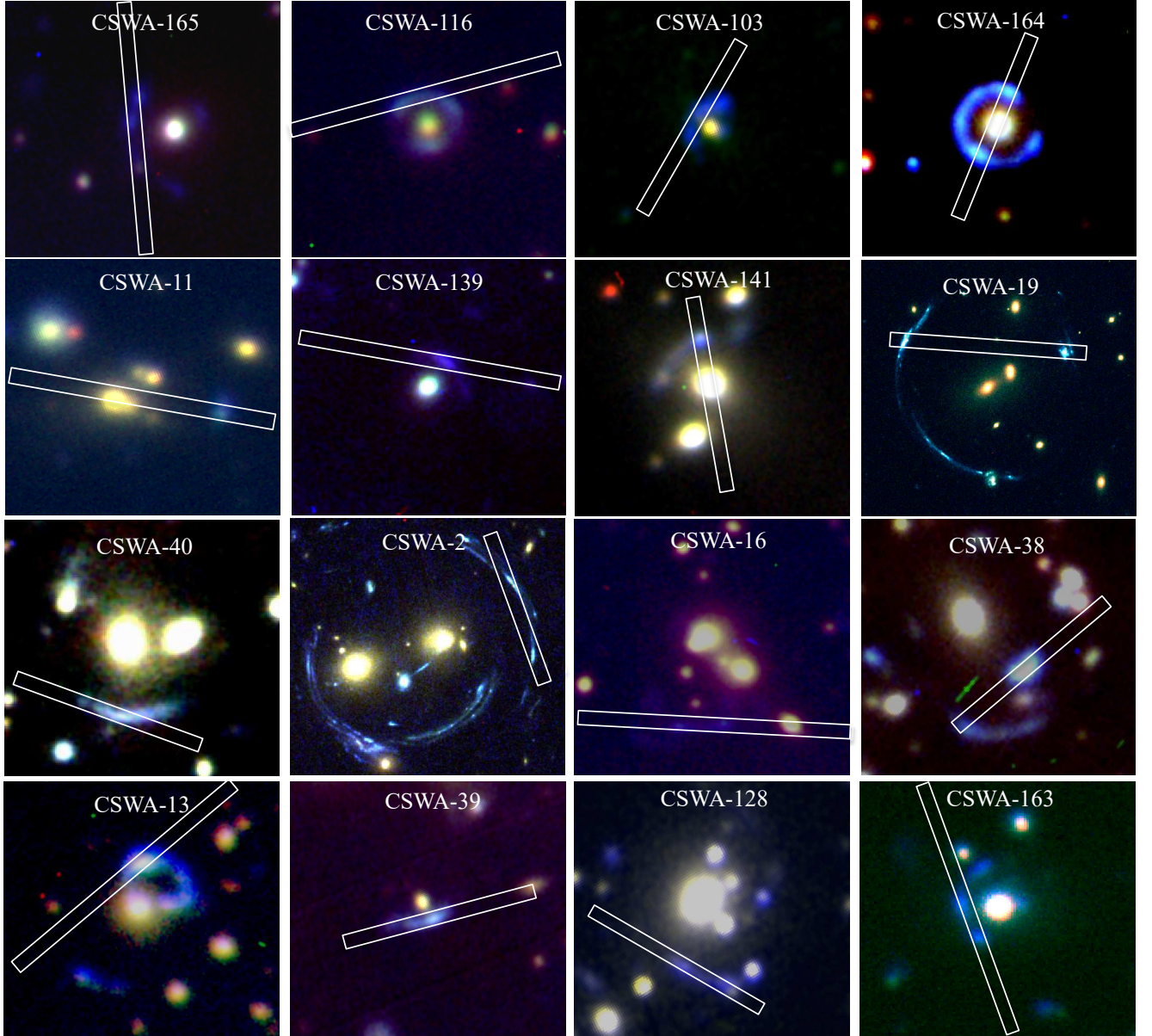


Figure 1. Color images of sixteen gravitationally lensed galaxies. The name of each sources is presented at the top of each image, along with the slit position used for the observations. For seven galaxies (CSWA-141, CSWA-13, CSWA-139, CSWA-116, CSWA-165, CSWA-164) the color images are created from g,r and i band images from LBT/MODS. The color images for four galaxies (CSWA-11,CSWA-163,CSWA-163,CSWA-103) are made with g,r and i bands images from LBT/LBC. Three color images (CSWA-38, CSWA-39, CSWA-40) are made using Keck/ESI images in V,R and I bands. For other two galaxies (CSWA-2, CSWA-19), color images are created using archival HST images. North is up and east is to the left. Each postage stamp is $25'' \times 25''$ in size. The orientation and centroid of the ESI or MMT slit is overlaid in each image.

centers (rest-frame). When the line is unresolved, we computed total CIII] emission line fluxes and associated line flux errors directly from the flux spectra and error spectra, respectively. If the line remained undetected at 3σ level, we calculated upper limits by integrating error spectrum from 1905 Å to 1912 Å. The emission line equivalent width is then computed by dividing the line fluxes (or upper limits) by median continuum level measured on either side of the CIII] line. We then searched for any other rest-UV emission features in the spectra and characterized them when detected. Our sample includes 10 galaxies with CIII] detection where the equivalent widths range from 0.4 Å to 4.6 Å (see Table 2). We will come

back to interpret the CIII] equivalent widths in §3.2, comparing the line strengths to optical line ratios and gas physical properties.

2.2.2 Near-Infrared Spectroscopy

Near-infrared (NIR) spectra supplement the optical spectra described above, providing constraints on the metallicity, ionization parameter, and electron density of the ionized gas. Near-infrared spectroscopic analysis is limited to the subset of sources from Table 1 which are located at redshifts placing strong rest-optical emission lines in spectral windows in which atmospheric transmission is near-unity. One of the sources in our sample (CSWA-2) was tar-

Object		EW (Å)		
	Ly α	[CIII] $\lambda 1907$	CIII] $\lambda 1909$	CIII] $\lambda 1908^a$
CSWA-141	...	2.3(1.3)	2.3(1.4)	4.6(1.9)
CSWA-13	5.4(2.1)	4.4(0.9)
CSWA-139	3.4(2.6)
CSWA-2	...	2.0(1.6)	1.1(0.9)	3.1(1.6)
CSWA-39	11.8(6.2)	0.6(0.1)	0.5(0.1)	1.1(0.2)
CSWA-19	...	0.4(0.1)	0.3(0.1)	0.7(0.1)
CSWA-38	2.6(1.1)	...	0.4(0.1)	
CSWA-128	...	0.3(0.1)	0.3(0.1)	0.6(0.1)
CSWA-103	...	0.3(0.1)	0.2(0.1)	0.5(0.1)
CSWA-164	2.0(0.5)	0.2(0.1)	0.2(0.1)	0.4(0.1)
CSWA-163	< 3.1
CSWA-16	< 2.3
CSWA-165	< 1.9
CSWA-40	...	< 1.2	< 1.2	< 1.7
CSWA-11	< 1.4
CSWA-116	< 1.1

^a Total CIII] doublet.

Table 2. Equivalent width measurements of rest-UV emission lines. The numbers within parentheses represent uncertainty. The upper limits are 3 σ .

Object	Dates	t _{exp} (ksec)	PA (deg)	Observatory/ Instrument
CSWA-165	2014 June 22	7.2	120	Magellen/FIRE
CSWA-164	2015 Nov 03	4.8	58	Magellen/FIRE
CSWA-11	2015 Nov 04	2.7	-10	Magellen/FIRE
CSWA-141	2012 Feb 15	1.2	280	Magellen/FIRE
CSWA-128	2012 Nov 7	3.6	190	LBT/LUCI
CSWA-163	2014 June 22	9.0	90	Magellen/FIRE

Table 3. Details of near-infrared spectroscopic observations obtained for this paper. From left to right, the columns denote the object ID, observation dates, exposure time, position angle of slit, and the observatory and instrument used to acquire near-IR spectroscopy. Further details are provided in §2.2.

geted with Keck near-infrared spectroscopy in Jones et al. (2013). In observing runs between November 2012 and November 2015, we have obtained near-infrared spectroscopic observations of five additional sources (CSWA-141, CSWA-164, CSWA-165, CSWA-163, CSWA-11) using the Folded-port InfraRed Echellette (FIRE; Simcoe et al. 2008) on the Magellan Baade Telescope. We used FIRE in its echelle mode, providing continuous spectral coverage spanning 0.82–2.51 μ m. We adopted a slit width of 0''.75, delivering a spectral resolution of 2.6 in the J band, 3.4 in the H band and 4.7 in the K band. Spectroscopic data reduction was performed using standard routines in the FIREHOSE data reduction pipeline¹.

One additional galaxy (CSWA-128) was observed on 2012 Nov 7 with the LUCI near-IR spectrograph on the Large Binocular Telescope (LBT). We used the N1.8 camera and 200_H+K grating in longslit mode. We first observed the lensed source with the HKSpec filter centered at 1.93 microns, providing spectral coverage from 1.50 to 2.30 μ m. We also observed CSWA-128 with the zJSpec filter centered at 1.1 microns, providing spectral coverage between 0.95 and 1.40 μ m. A slit width of 1''.0 was used, resulting in a spectral resolution of 16. Spectroscopic data reduction was performed using standard IDL long slit reduction packages (see Bian et al. 2010 for

¹ wikis.mit.edu/confluence/display/FIRE/FIRE+Data+Reduction

details). We summarize details of near-infrared spectroscopy of CASSOWARY galaxies in Table 3. Example spectra are shown in Figure 3.

Emission line fluxes in the NIR spectra are measured using the IDL routine MPFITPEAK which computes line fluxes after fitting a gaussian model. In cases where the emission lines are partially affected by a skyline, we mask the contaminated region before fitting the emission line. Additionally, if one of the components of [OIII] $\lambda\lambda 4959,5007$ is strongly affected by an emission line, we assume the theoretical line ratio of [OIII] $\lambda 5007$ /[OIII] $\lambda 4959$ =2.98 (Storey & Zeippen 2000) in calculating the total [OIII] line flux.

We calculate the impact of dust on the nebular lines using the Balmer decrement flux ratio of H α /H β . The observed line ratio is compared to the line ratio expected in absence of dust (H α /H β =2.86; Osterbrock & Ferland 2006) for case B recombination assuming T_e=10,000 K. In the two cases where the Balmer line ratios are not available, we use the stellar reddening inferred from the broadband data to estimate the nebular attenuation (see §2.5). We note that using stellar reddening for nebular attenuation correction doesn't impact our results. We assume that the nebular gas attenuation is similar to the stellar continuum attenuation. We presented the observed and dust-corrected emission line measurements in Table 4.

For one object (CSWA-141) where auroral [OIII] $\lambda 4363$ line is detected, we calculated electron temperature using PyNeb (version 1.1.8; Luridiana et al. 2015) using emission line flux ratio of OIII] $\lambda 4363$ /[OIII] $\lambda 5007$. For our calculations, we adopted the default PyNeb atomic data sets. We assumed electron density of 250 cm⁻³, which is typical to $z \sim 2$ galaxies (Sanders et al. 2016a). However, we note that our assumed electron density value has negligible effect on the derived electron temperature in the low density regime ($< 10^3$ cm⁻³). Since we don't have T_e([OII]) sensitive emission line measurements, we followed the relation given by Izotov et al. (2006) for low metallicity to estimate the electron temperature in the O⁺² region. We use our electron temperature measurements to infer the direct oxygen abundance. We only use O⁺/H⁺ and O⁺²/H⁺ to compute oxygen abundance since the ionization states higher than O⁺² contributes significantly low at less than 1 per cent (Izotov et al. 2006). O⁺/H⁺ and O⁺²/H⁺ are calculated from PyNeb using our T_e([OIII]), T_e([OII]), n_e and emission line fluxes of [OII], H β and [OIII].

We use PyNeb to calculate the electron density using the flux ratio of the [OII], [SII], and [CIII], CIII] doublets. The typical error in measurements is then calculated using the errors in emission line fluxes. When an electron temperature measurement is not available, we assumed electron temperature of 10,000K following Sanders et al. (2016a) to adopt temperature dependent effective collision strengths. Adopting electron temperature of 7000K (15000K) instead would overestimate (underestimate) electron density by 15–20% which is effectively lower than density error from our line flux measurements.

2.3 Imaging

Each of the CASSOWARY galaxies was discovered in SDSS imaging. In many cases, the photometric constraints from SDSS are unreliable owing to blending with neighbors and low S/N detection of diffuse emission associated with the arcs. We have obtained deeper optical multi-band imaging for each of the galaxies discussed in this paper using cameras on the LBT and Keck. In order to better characterize the stellar populations, we have also obtained near-IR imaging sampling across the Balmer break for a subset of our targets using the LBT, MMT and Keck. In the following subsections,

Line	$\lambda_{\text{rest}}(\text{\AA})$	$\lambda_{\text{obs}}(\text{\AA})$	$F(\lambda)/F(5007)$	$I(\lambda)/I(5007)$
CSWA-141				
[OII]	3727.13	9039.2	0.060 ± 0.002	0.088 ± 0.003
[OII]	3729.92	9045.9	0.075 ± 0.004	0.110 ± 0.006
[NeIII]	3869.66	9384.9	0.054 ± 0.017	0.075 ± 0.023
H δ	4102.90	9950.5	0.030 ± 0.004	0.039 ± 0.005
H γ	4341.58	10529.4	0.063 ± 0.003	0.076 ± 0.004
[OIII]	4365.31	10586.9	0.019 ± 0.002	0.023 ± 0.002
H β	4862.55	11792.9	0.13 ± 0.003	0.135 ± 0.003
[OIII]	4960.25	12029.8	0.338 ± 0.004	0.342 ± 0.004
[OIII]	5008.27	12146.3	1.000	1.000
[SIII]	6310.48	15304.4	0.007 ± 0.001	0.005 ± 0.001
[NII]	6549.84	...	< 0.004	< 0.002
H α	6564.61	15920.7	0.529 ± 0.003	0.386 ± 0.002
[SII]	6717.96	16292.7	0.017 ± 0.001	0.013 ± 0.001
[SII]	6732.34	16327.5	0.016 ± 0.001	0.012 ± 0.001
CSWA-165				
[OII]	3727.13	11657.1	0.56 ± 0.06	1.01 ± 0.11
[OII]	3729.92	11665.9	0.63 ± 0.08	1.13 ± 0.14
[NeIII]	3869.66	...	< 0.23	< 0.38
H β	4862.55	15208.9	0.46 ± 0.08	0.49 ± 0.08
[OIII]	5008.27	15665.2	1.00	1.00
H α	6564.61	20532.4	2.25 ± 0.15	1.40 ± 0.09
[NII]	6585.28	20597.5	0.55 ± 0.09	0.34 ± 0.06
CSWA-165				
[OII]	3727.13	11482.5	0.28 ± 0.01	0.53 ± 0.02
[OII]	3729.92	11491.2	0.35 ± 0.03	0.66 ± 0.06
[NeIII]	3869.66	...	< 0.04	< 0.07
H γ	4341.58	13375.6	0.06 ± 0.03	0.08 ± 0.04
H β	4862.55	14981.5	0.22 ± 0.03	0.23 ± 0.03
[OIII]	4960.25	15282.5	0.35 ± 0.02	0.35 ± 0.02
[OIII]	5008.27	15429.9	1.00	1.00
H α	6564.61	20225.5	1.12 ± 0.04	0.67 ± 0.02
[NII]	6585.28	20289.2	0.18 ± 0.06	0.11 ± 0.04
CSWA-163				
[OII]	3727.13	11482.5	0.28 ± 0.01	0.53 ± 0.02
[OII]	3729.92	11491.2	0.35 ± 0.03	0.66 ± 0.06
[NeIII]	3869.66	...	< 0.04	< 0.07
H γ	4341.58	13375.6	0.06 ± 0.03	0.08 ± 0.04
H β	4862.55	14981.5	0.22 ± 0.03	0.23 ± 0.03
[OIII]	4960.25	15282.5	0.35 ± 0.02	0.35 ± 0.02
[OIII]	5008.27	15429.9	1.00	1.00
H α	6564.61	20225.5	1.12 ± 0.04	0.67 ± 0.02
[NII]	6585.28	20289.2	0.18 ± 0.06	0.11 ± 0.04
CSWA-128				
[OII]	3729.01	12019.6	0.28 ± 0.08	0.40 ± 0.11
[NeIII]	3869.66	12476.4	0.10 ± 0.03	0.14 ± 0.04
H β	4862.55	15681.7	0.24 ± 0.06	0.25 ± 0.06
[OIII]	4960.25	15997.7	0.32 ± 0.04	0.33 ± 0.04
[OIII]	5008.27	16151.8	1.00	1.00
[NII]	6549.84	21121.3	0.05 ± 0.01	0.04 ± 0.01
H α	6564.61	21170.3	0.96 ± 0.05	0.71 ± 0.04
[NII]	6585.28	21237.2	0.13 ± 0.02	0.09 ± 0.01
[SII]	6717.96	21664.9	0.10 ± 0.02	0.07 ± 0.01
[SII]	6732.34	21711.1	0.08 ± 0.04	0.06 ± 0.02
CSWA-164				
[OII]	3727.13	13090.9	0.52 ± 0.11	0.80 ± 0.17
[OII]	3729.92	13100.4	0.64 ± 0.04	0.99 ± 0.07
[OIII]	5008.27	17590.4	1.00	1.00
H α	6564.61	23064.8	1.91 ± 0.09	1.34 ± 0.06
CSWA-11				
[OII]	3727.13	8979.9	0.67 ± 0.13	0.85 ± 0.16
[OII]	3729.92	8986.6	0.66 ± 0.09	0.83 ± 0.11
[NeIII]	3869.66	...	< 0.43	< 0.53
[OIII]	5008.27	12068.7	1.00	1.00
H α	6564.61	15816.5	1.08 ± 0.06	0.89 ± 0.05

Table 4. Rest-optical emission line measurements of six bright lensed Cassowary galaxies. Measurements are from Magellan/FIRE (CSWA-141, CSWA-165, CSWA-163, CSWA-164, CSWA-11) and LBT/LUCI (CSWA-128). Line flux measurements are quoted relative to [OIII] $\lambda 5007$. We adopt [OIII] $\lambda 5007$ as a reference line due to its high S/N. Three-sigma upper limits are reported for emission lines that are not detected.

Object	Observatory / Instrument	Filters Observed	Dates	t_{exp} (sec)
CSWA-165	LBT/MODS	g	2014 Jan 27	720
	LBT/MODS	r, z	2014 Jan 27	360
	MMT/MMIRS	J	2015 Sep 30	900
	MMT/MMIRS	K	2015 Sep 30	1200
	LBT/MODS	g	2014 Jan 27	720
	LBT/MODS	r, z	2014 Jan 27	360
	MMT/MMIRS	J, K	2015 Oct 01	600
	LBT/LBC	g	2015 Nov 15	600
	LBT/LBC	r, i	2015 Nov 15	300
	MMT/MMIRS	J, K	2015 Oct 01	600
CSWA-103	LBT/MODS	g	2014 Jan 27	720
	LBT/MODS	r, z	2014 Jan 27	360
CSWA-164	LBT/LBC	g	2015 Nov 15	600
	LBT/MODS	r, z	2014 Jan 27	360
CSWA-11	LBT/LBC	g	2015 Nov 15	600
	LBT/LBC	r, z	2015 Nov 15	300
Keck/ MOSFIRE	Keck/ MOSFIRE	K _s	2015 Nov 30	300
	LBT/MODS	g	2014 Jan 27	720
CSWA-139	LBT/MODS	r, z	2014 Jan 27	360
	MMT/MMIRS	H	2017 Jan 11	900
CSWA-141	LBT/ MODS	g	2014 Jan 27	720
	LBT/ MODS	r, z	2014 Jan 27	360
Keck/ MOSFIRE	Keck/ MOSFIRE	K _s	2014 Apr 11	300
	Keck/ MOSFIRE	Y	2015 Nov 30	300
Keck/ MOSFIRE	Keck/ MOSFIRE	J ₂	2015 Nov 30	300
	Keck/ESI	V, R, I	2013 Mar 06	200
CSWA-16	LBT/MODS	g, r	2014 Jan 27	360
	Keck/ESI	V, R, I	2013 Mar 06	200
CSWA-38	LBT/MODS	g	2014 Jan 27	720
	LBT/MODS	r, z	2014 Jan 27	360
CSWA-13	LBT/LUCI	K _s	2014 Apr 13	1200
	MMT/MMIRS	V, R, I	2013 Mar 06	200
CSWA-39	LBT/LBC	g	2015 Nov 15	600
	LBT/LBC	r, i	2015 Nov 15	300
Keck/ MOSFIRE	Keck/ MOSFIRE	K _s	2014 Apr 11	300
	LBT/LBC	g	2015 Nov 15	600
CSWA-163	LBT/LBC	r, i	2015 Nov 15	300
	MMT/MMIRS	J	2015 Sep 30	900
MMT/MMIRS	MMT/MMIRS	K	2015 Sep 30	1200

Table 5. New optical and near-infrared imaging of CASSOWARY lensed galaxies obtained with Keck, LBT, and MMT. From left to right, columns denote the object ID, observatory and instrument, filters utilized, dates of observations, and exposure time.

we describe the optical and near-infrared imaging observations and analysis. Details of the new imaging observations are summarized in Table 5.

2.3.1 Optical imaging

We secured images of seven galaxies from Table 1 using the Multi Object Double Spectrograph (MODS, [Pogge et al. 2010](#)) on LBT in January 2014. The dual channel mode of MODS provides images in two separate filters simultaneously over a field of view of 6×6 arc minutes. We used the blue and red channel to obtain g, r, and z-band images for CSWA-13, CSWA-16, CSWA-116, CSWA-139, CSWA-141, CSWA-164 and CSWA-165. Each arc was first observed in the g and r-band for 360 seconds and then in the g and z-band for an additional 360 seconds. For one source (CSWA 16), we obtained imaging only in the g and r-bands. The sky was partly covered by clouds throughout the MODS observations and the seeing varied between $1.^{\prime\prime}0$ and $1.^{\prime\prime}5$. Optical images of three

other galaxies (CSWA-39, CSWA-38, CSWA-40) were taken with ESI on Keck, providing a field of view of 2×3.5 arc minutes. These three sources were observed with V, R and I filters. There was some cloud during the observations, and the seeing was between $0''.8$ and $1''.2$. For the two other sources in Table 1, CSWA-2 and CSWA-19, we make use of archival HST images (program 11974, PI: Allam). We summarize the details of the imaging observations in Table 5.

The optical images were reduced using standard routines for flat fielding and image combination. The 5σ typical limiting magnitude in the g, r and z bands of MODS images are 25.5, 24.7 and 23.2 respectively. Similarly, for the ESI images the typical 5σ limiting magnitude in V, R and I bands are 22.7, 22.6 and 22.6 respectively. For the archival HST images, the typical 5σ limiting magnitudes in F450W, F606W, and F814W filters are 26.3, 26.1 and 25.5 respectively. Each image was flux calibrated using stars that are isolated and well detected in SDSS imaging. The mosaic in Figure 1 shows the multi-color optical imaging obtained for each source.

Before performing photometry on the lensed galaxies, we modeled the foreground lens using GALFIT (Peng et al. 2002) and subtracted its contribution to the lensed source. To calculate the absolute magnitude for the galaxies in our sample, we first measured the integrated flux in the g-band. After applying the appropriate magnification corrections (see §2.4), we arrive at the absolute UV magnitudes shown in Table 1. The values span $M_{UV} = -23.1$ to $M_{UV} = -20.4$, corresponding to $0.8\text{-}9 L_{UV}^*$ at $z \approx 2 - 3$ (Reddy & Steidel 2009; Parsa et al. 2016).

2.3.2 Near-infrared imaging

We obtained near-infrared images of CSWA-141, CSWA-11 and CSWA-128 in the K_s -band using the Multi-Object Spectrometer for Infra-Red Exploration (MOSFIRE, McLean et al. 2012) on Keck I. Conditions were photometric with seeing of $0''.5$. We obtained 10 dithered frames having 6.1×6.1 arc minute field of view, each with exposure time of 30 seconds. The 5σ AB limiting magnitude in the MOSFIRE K_s -band images is 23.1. With the goal of constraining the equivalent width of [OIII] and H-beta emission, we observed CSWA-141 with the MOSFIRE J2 medium band filter. The filter spans $1.11\text{-}1.25 \mu\text{m}$, covering H-beta and [OIII].

We secured a K_s -band image of CSWA-13 using the LUCI near-IR Spectrograph on the LBT when the seeing was $1''.2$. We utilized the N3.75 camera providing 4×4 arc minutes of field of view with a plate scale of 0.12 arcseconds per pixel. The near-IR imaging reduction was performed using standard IDL routines designed to flat field, sky-subtract and stack the dithered frames. Finally, we used isolated and unsaturated stars that are in the 2MASS catalog to flux calibrate the images. The 5σ AB limiting magnitude in the LUCI K_s -band image is 23.4. For another four galaxies (CSWA-116, CSWA-165, CSWA-103, CSWA-163), near-IR imaging was obtained using the MMIRS instrument on the MMT. Each of the four sources was observed in the J and K bands. MMIRS provides imaging over a field of view of 6.9×6.9 arc minutes with a plate scale of 0.20 arcsec per pixel. The seeing was between $0''.6\text{-}0''.9$ throughout the observations. The typical 5σ AB limiting magnitude in MMIRS J and K-band images are 22.9 and 22.8, respectively.

2.4 Lensing Magnification

Derivation of stellar mass and intrinsic luminosity of lensed systems requires magnification correction. In Stark et al. (2013b), magnification factors were presented for eleven out of sixteen sources

given in Table 1 and typically range between $\mu=5$ and 10. Three out of the five remaining sources have a published lens model. We adopted magnifications for CSWA-38 and CSWA-39 from Koester et al. (2010) and CSWA-11 from Leethochawalit et al. (2016).

For the two remaining sources (CSWA-13 & CSWA-16), we follow a similar approach to Hezaveh et al. (2013). In brief, we assumed a symmetric Gaussian light distribution for the lensed source. We also tested the impact of adding a second Gaussian component to the source. The foreground lens is modeled as a Singular Isothermal Ellipsoid (SIE). Multiple lenses are allowed in the modeling procedure. To obtain the best fit model, we perform a Markov Chain Monte Carlo (MCMC) analysis to minimize χ^2 in the image plane. In the case of CSWA-16, the observed data are better fit after introducing a second Gaussian component to the background source. The magnification factor is then calculated as the ratio of the lensed to unlensed flux. We derive a magnification of $\mu = 3.9 \pm 0.3$ for CSWA-16 and $\mu = 1.9 \pm 0.2$ for CSWA-13.

2.5 Stellar Population Synthesis Modeling

Thirteen of the galaxies shown in Figure 1 have the necessary optical and near-IR imaging to derive physical properties from broadband SED fitting. For these systems, we infer the stellar mass, specific star formation rate and dust attenuation using the Bayesian galaxy SED modeling and interpreting tool BEAGLE tool (version 0.20.3; Chevallard & Charlot 2016). BEAGLE is based on the photoionization models of star-forming galaxies in Gutkin et al. (2016), combining the latest version of the Bruzual & Charlot (2003) stellar population synthesis models with the photoionization code CLOUDY (Ferland et al. 2013).

We fit the broadband photometric fluxes as well as CIII] equivalent widths. When relative fluxing between rest-UV and optical emission lines is possible, we include all emission lines in the fitting procedure. The models assume constant star formation where the maximum stellar age is allowed to vary freely between 5 Myr to the Universe age at the given redshift. We use Chabrier (2003) initial mass function and the Calzetti et al. (2000) extinction curve. The metallicity is allowed to vary in the range of $-2.2 \leq \log(Z/Z_{\odot}) \leq 0.25$ assuming equivalent stellar and nebular metallicity ($Z_{\star}=Z_{ISM}$). The redshift of all objects is fixed to their spectroscopic redshift given in Table 1. The ionization parameter (U_S ; here defined as the ratio of ionizing-photon to gas densities at the edge of the Strömgren sphere) is varied in the range of $-4.0 \leq U_S \leq -1.0$, and the dust-to-metal mass ratio spanned within the range of $\xi_d=0.1\text{-}0.5$. We adopt models with hydrogen density ($n_H=100 \text{ cm}^{-3}$) and C/O abundance of 0.5 of solar value $[(\text{C}/\text{O})_{\odot} \approx 0.44]$. Finally, the prior on the V-band dust attenuation optical depths ($\hat{\tau}_V$) is taken as an exponential distribution after fixing the fraction of attenuation optical depth arising from the ambient ISM (μ) to be 0.4. We note that our assumption of constant star formation may underestimate the stellar mass by as high as 0.5 dex when the galaxy is dominated by a young stellar population, but this would not affect the primary conclusions of this paper. We discuss the main results of this SED fitting in §3.2.

3 RESULTS

All sixteen sources presented in this paper have optical spectra covering CIII] to quantify equivalent widths. We report these values (or 3σ upper limits) in Table 2. Of the sixteen sources, six galaxies have near-IR spectra enabling rest optical line flux ratios (Table 3).

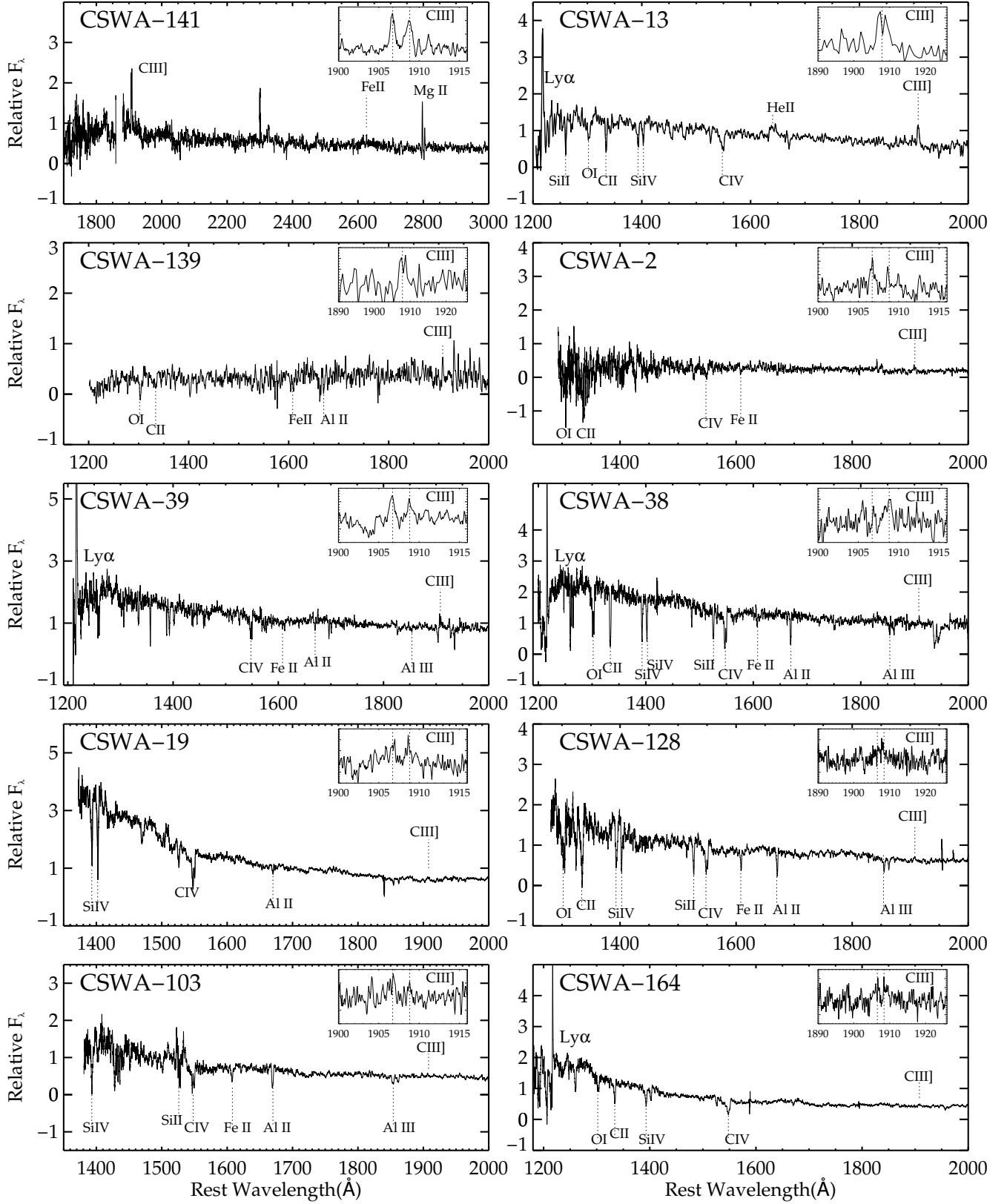


Figure 2. Rest-UV spectra of gravitationally lensed galaxies presented in Table 1 with CIII] detections. The upper left side of each image contains the CASSOWARY-ID. The dotted dashed line below and above the UV continuum represents absorption and emission features identified in the spectra. The upper right of each panel shows zoom in spectral coverage near CIII] $\lambda\lambda$ 1907,1909. The vertical dashed lines in the inset show the location of CIII] $\lambda\lambda$ 1907,1909 doublet. The CIII] doublet remain unresolved in the MMT/BCS spectra of CSWA-13 and CSWA-139.

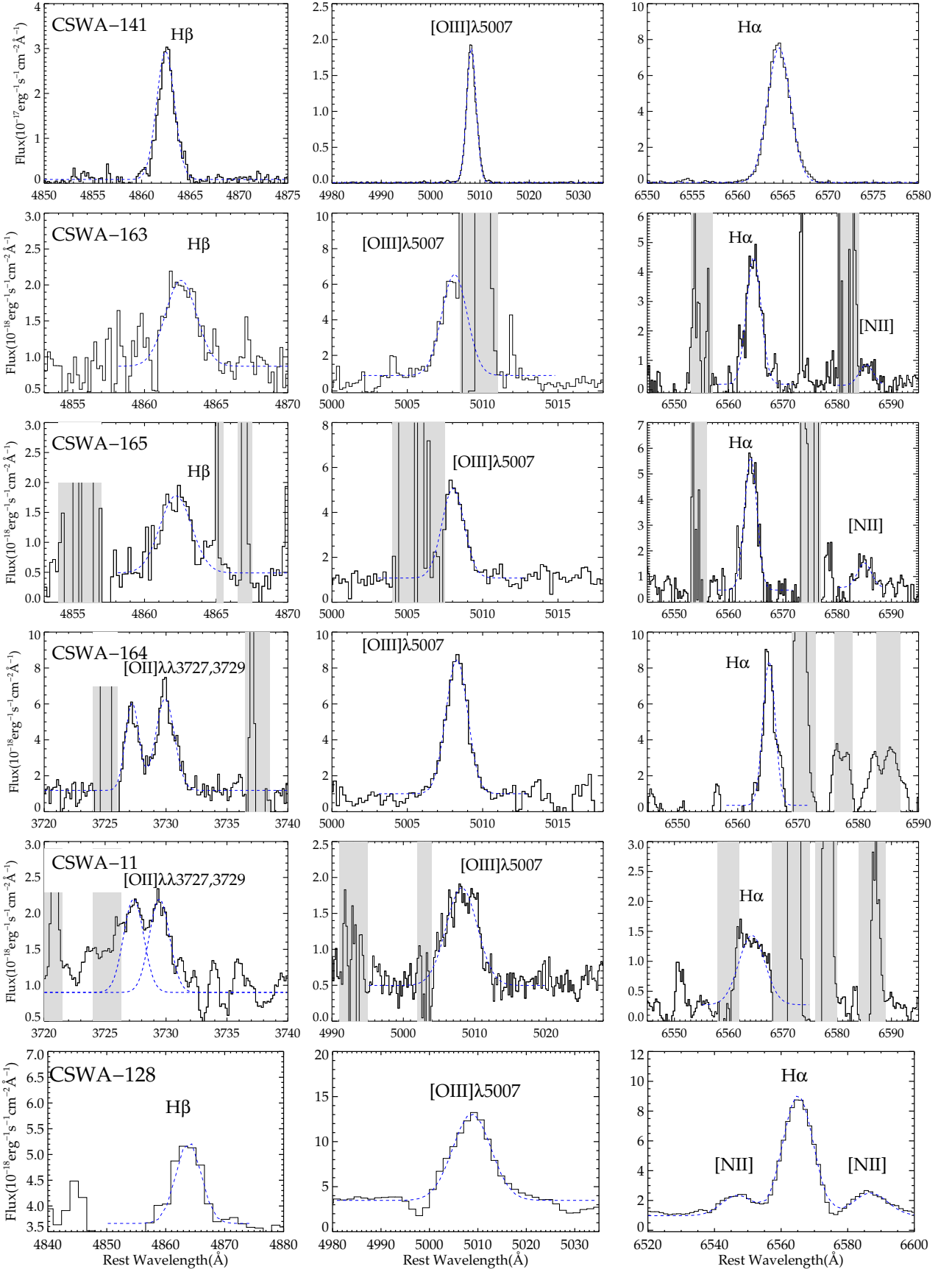


Figure 3. Optical emission lines in six gravitationally lensed galaxies discussed in this paper. Each row shows optical emission lines from a single source. The object ID is given in the leftmost panel of each row. The black line represents observed flux whereas blue line shows gaussian fit to the line profile calculated using IDL routine MPFITPEAK. The region affected by sky lines is shown as a grey swath.

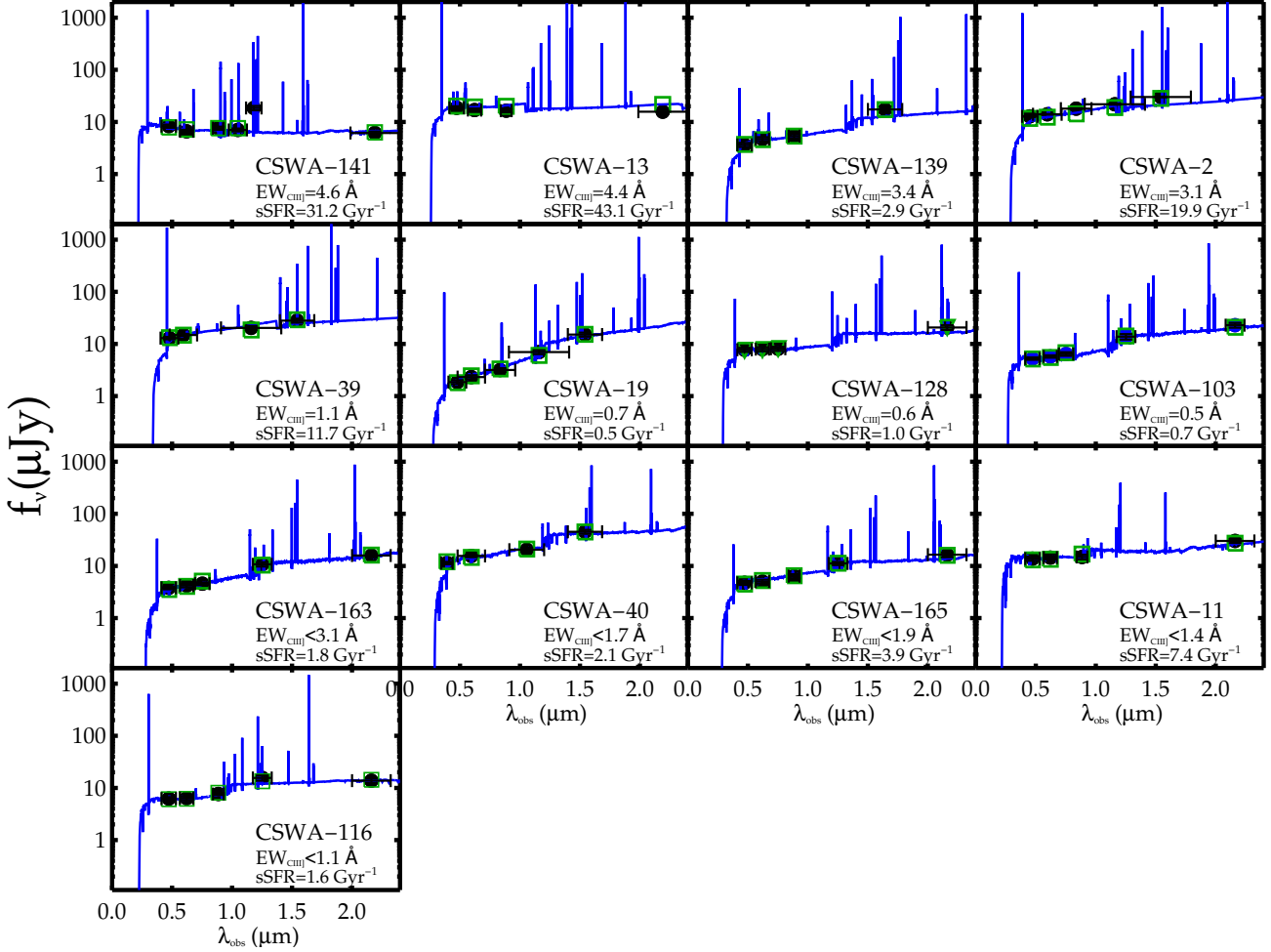


Figure 4. SEDs of galaxies in the sample. The black circle represents broad band photometry data, blue line represents best fit population synthesis model to the observed data (see §2.5) and green square shows synthetic broad band flux from the best fit model. The lower right of each panel shows object ID, sSFR and CIII] equivalent widths.

Object	$\log(M_*/M_\odot)$	sSFR (Gyr $^{-1}$)	τ_V
CSWA-141	$8.6^{+0.2}_{-0.3}$	$31.2^{+60.8}_{-16.3}$	$0.17^{+0.18}_{-0.12}$
CSWA-13	$9.8^{+0.3}_{-0.3}$	$43.1^{+56.6}_{-28.7}$	$0.53^{+0.13}_{-0.17}$
CSWA-139	$10.3^{+0.5}_{-0.3}$	$2.9^{+14.3}_{-2.0}$	$0.77^{+0.41}_{-0.33}$
CSWA-2	$9.1^{+0.3}_{-0.3}$	$19.9^{+26.1}_{-10.4}$	$0.96^{+0.31}_{-0.27}$
CSWA-39	$9.9^{+0.3}_{-0.3}$	$11.7^{+13.8}_{-13.8}$	$0.96^{+0.31}_{-0.31}$
CSWA-128	$9.9^{+0.4}_{-0.1}$	$1.0^{+0.4}_{-0.3}$	$0.13^{+0.06}_{-0.07}$
CSWA-19	$10.5^{+0.1}_{-0.1}$	$0.5^{+0.4}_{-0.1}$	$1.09^{+0.21}_{-0.16}$
CSWA-103	$10.4^{+0.2}_{-0.2}$	$0.7^{+0.1}_{-0.3}$	$0.48^{+0.31}_{-0.23}$
CSWA-163	$9.9^{+0.1}_{-0.1}$	$1.8^{+0.9}_{-0.9}$	$0.67^{+0.09}_{-0.13}$
CSWA-40	$10.8^{+0.2}_{-0.2}$	$2.1^{+3.3}_{-1.3}$	$0.43^{+0.29}_{-0.25}$
CSWA-165	$10.0^{+0.2}_{-0.2}$	$3.9^{+3.0}_{-1.9}$	$0.62^{+0.12}_{-0.13}$
CSWA-11	$10.0^{+0.4}_{-0.3}$	$7.4^{+14.0}_{-5.5}$	$0.28^{+0.31}_{-0.20}$
CSWA-116	$9.4^{+0.2}_{-0.2}$	$1.3^{+2.4}_{-0.7}$	$0.27^{+0.34}_{-0.18}$

Table 6. Physical properties inferred from BEAGLE fitting for subset of CASSOWARY galaxies with optical and near-IR photometry. From left to right, the columns give the object name, C III] equivalent widths, magnification corrected stellar mass, specific star formation rates and V-band optical depth.

Ten sources have multi-wavelength photometry with SED information enabling stellar mass and sSFR measurements. Below we briefly comment on individual galaxy properties where sources are ordered by descending CIII] equivalent width.

3.1 Notes on Individual Sources

CSWA-141 is an extreme equivalent width optical line emitting galaxy at $z = 1.425$ with an integrated apparent magnitude of $r = 20.7$. The Magellan/FIRE spectrum reported in Stark et al. (2013a) shows a large number of rest-frame optical emission lines, including the temperature sensitive [OIII] $\lambda\lambda 4363$ auroral line and the density sensitive [SII] $\lambda\lambda 6717, 6731$ and [OII] $\lambda\lambda 3727, 3730$ lines (see Figure 3). We have since obtained deep Keck/ESI and LBT/MODS optical spectra and optical and near-IR imaging, providing constraints on the rest-UV metal lines and the SED.

The optical to near-infrared SED of CSWA-141 (Figure 4) implies a very large specific star formation rate (sSFR= 31^{+61}_{-16} Gyr $^{-1}$). After correcting for magnification due to lensing ($\mu=5.5$), the stellar mass and star formation rate of the best fitting model are $3.98 \times 10^8 M_\odot$ and $12^{+24}_{-7} M_\odot \text{ yr}^{-1}$, respectively (Table 6). The flux in the medium-band J2 MOSFIRE filter (covering 1.117 to 1.246 μm) is significantly in excess of that in adjacent filters, as expected given the

Line	λ_{rest} (Å)	λ_{obs} (Å)	F_{line} $F_{\text{CIII}]\lambda 1909}$	EW (Å)
Keck/ESI				
[CIII]	1906.73	4624.32	1.02(0.10)	2.3(1.3)
CIII]	1908.68	4628.84	1.00	2.3(1.4)
Fe II*	2626.64	6370.24	0.22(0.07)	0.9(0.5)
Mg II	2796.36	6783.42	1.30(0.07)	9.7(6.8)
	2803.53	6800.79	0.65(0.04)	4.8(2.6)
[OII]	3727.10	9039.02	5.10(0.04)	26.3(12.4)
	3729.86	9045.68	6.62(0.09)	39.2(19.9)
[NeIII]	3870.16	9385.28	4.79(0.23)	19.5(13.8)
LBT/MODS				
Line	λ_{rest} (Å)	λ_{obs} (Å)	F_{line} $F_{\text{CIII}]\lambda 1909}$	EW (Å)
[CIII]	1908	4622.13	1.00	3.5(1.5)
He II	1640.52	3974.16	< 0.08	< 0.7
CIV	1549	3758.75	< 0.11	< 0.8
OIII]	1660.81	4027.93	0.09(0.02)	0.3(0.2)
	1666.15	4040.15	0.23(0.03)	0.7(0.2)
Si III]	1882.98	4566.25	0.24(0.03)	0.7(0.1)
Si III]	1892.03	4588.16	0.11(0.02)	0.3(0.1)

Table 7. Rest-UV emission line measurements of CSWA-141. Emission line fluxes are presented relative to the CIII] $\lambda 1909$ line flux for the Keck/ESI data, while the line fluxes are presented relative to unresolved combined CIII] flux for LBT/MODS data. The upper limits are 3σ .

contamination by extremely strong [OIII] and H β lines. We use the J2 flux excess to calculate the equivalent width from [OIII] and H β , following the methodology adopted at higher redshift (e.g., Stark et al. 2013b; Smit et al. 2015). This approach yields a rest-frame equivalent width of $W_{\text{[OIII]}+\text{H}\beta} = 730$ Å, consistent with the very young stellar populations (32 Myr for constant star formation) implied by the population synthesis modeling. While the optical line EW is significantly in excess of what is seen in typical star forming galaxies at $z \approx 2$ (e.g., Boyett et al. 2022), it is nearly identical to the average [OIII]+H β EW at $z \approx 7 - 8$, as implied by flux excesses in *Spitzer*/IRAC bandpasses (Labbé et al. 2013; Smit et al. 2015; De Barros et al. 2017; Endsley et al. 2020). The continuum brightness of CSWA-141 enables a unique and detailed view of this population.

The ESI spectrum covers 4100-10000 Å, revealing prominent emission from [CIII] $\lambda 1907$, CIII] $\lambda 1909$, Fe II* $\lambda 2626$, Mg II $\lambda 2797,2804$, [OII] $\lambda 3726,3729$, [Ne IIII] $\lambda 3869$, and H δ (Table 7). The [CIII], CIII] doublet is easily resolved by ESI (Figure 2) with a total rest-frame equivalent width of $W_{\text{CIII}]} = 4.6$ Å, the largest of the sixteen galaxies considered in this paper. Nebular Mg II emission also exhibits a very large rest-frame equivalent width ($W_{\text{MgII}} = 15.0$ Å), as is common in lower mass galaxies (e.g., Erb et al. 2012; Guseva et al. 2019). The MODS spectrum provides better blue sensitivity than ESI, yielding detection of OIII] $\lambda 1661,1666$ and Si III] $\lambda 1883,1892$. The CIII] doublet is also detected, but it is unresolved at the resolution of MODS (Figure 5). The summed equivalent widths of the OIII] and Si IIII] doublet (1.0 Å and 1.0 Å, respectively) are considerably lower than CIII] (see Table 7). The high ionization lines He II $\lambda 1640$ and CIV] $\lambda 1548,1550$ are not detected, implying rest-frame equivalent widths below 0.3 and 0.5 Å (at 3σ), respectively. For emission lines detected by both ESI and MODS, we will adopt whichever instrument provides the higher S/N EW measurement for our subsequent analysis and discussion.

The rest-frame optical emission lines detected in the FIRE spectrum provide an array of constraints on the nebular gas physical conditions. The detection of [OIII] $\lambda 4363$ in the FIRE spectrum enables a measure of the nebular electron temperature ($T_e = 1.5 \pm 0.1 \times 10^4$ K) and the oxygen abundance via the direct T_e method. Following the process discussed in §2.2.3, we find that $12 + \log(\text{O/H}) = 7.95 \pm 0.08$, implying a gas-phase metallicity of $0.18 Z_\odot$. Our measurement is very similar to Sanders et al. (2016b) who reported oxygen abundance ($12 + \log(\text{O/H})$) of CSWA-141 based on our line flux measurements given in Table 4. The derived metallicity is also consistent with the metallicities derived from the N2 and O3N2 indices with the calibration presented in Bian et al. (2018) ($12 + \log(\text{O/H}) < 8.0$).

The O32 (6.6) and R₂₃ indices (11.4) point to a large ionization parameter and gas excitation. The exact values depend on the input ionizing spectrum. Photoionization modeling using BEAGLE resulted in a large ionization parameter of $\log U_s = -2.1 \pm 0.1$, which is broadly consistent with O₃₂ vs ionization parameter relationships in the literature (e.g., Sanders et al. 2016a; Berg et al. 2019). The photoionization modeling further suggested a high ionizing photon production efficiency of $\log(\xi_{\text{ion}}/\text{Hz erg}^{-1}) = 25.5 \pm 0.1$. This is higher than the canonical value typically assumed for galaxy-driven reionization model (Robertson et al. 2010) but consistent with other strong CIII] emitters in the literature (e.g., Nakajima et al. 2018). While the measured O₃₂ and R₂₃ are rare among more massive star-forming galaxies at $z \approx 2$, they are consistent with the O₃₂-sSFR and O₃₂-R₂₃ trends that are observed at high redshift (e.g., Sanders et al. 2016a; Strom et al. 2016).

The electron densities inferred from the flux ratios of the [OII] and [SII] doublets using PyNeb (160_{-74}^{+76} cm $^{-3}$ and 350_{-206}^{+294} cm $^{-3}$, respectively) are consistent with the median density of more massive star forming galaxies at $z \approx 2$ (250 cm $^{-3}$; e.g., Sanders et al. 2016a). In contrast, the resolved [CIII], CIII] doublet suggests gas at very high density (16500_{-7800}^{+12100} cm $^{-3}$). Such an offset between densities derived from CIII] and those inferred from [OII], [SII] have been seen in other galaxies at high redshift (e.g., James et al. 2014). We will come back to discuss this in more detail in §4.

Finally, we note that the MODS and FIRE spectra reveal emission lines at 3827, 15304, 15612, 15763, 20663 Å which appear nearly spatially coincident with CSWA-141 but are not associated with the $z = 1.425$ galaxy (see Figure 5). We identify these as Ly α , H β , [OIII] $\lambda\lambda 4959,5007$, and H α in a second fainter gravitationally lensed source at $z = 2.148$. This higher redshift galaxy is unresolved from the $z = 1.425$ source in existing ground-based optical and near infrared images. Given that the H α flux of the $z = 1.425$ galaxy is $7.4 \times$ larger than the $z = 2.148$ source, we expect that the newly-discovered higher redshift source contributes negligibly (at the 5% level) to the broadband flux and the rest-UV continuum in the MODS and ESI spectra. Higher resolution imaging will be required to disentangle the two sources.

CSWA-13 is a bright galaxy at $z = 1.87$ that was first confirmed in Stark et al. (2013a) through the detection of Ly α emission and numerous interstellar absorption lines in an MMT blue channel spectrum. CIII] emission is confidently detected ($W_{\text{CIII}]} = 4.4 \pm 0.9$ Å) in the discovery spectrum. He II is also detected ($W_{\text{HeII}} = 4.3 \pm 0.9$ Å) with a broad FWHM (2430 km s $^{-1}$) that is indicative of a stellar wind origin. We do not detect the OIII] doublet, implying individual components with equivalent widths less than 0.8 Å. While this is among the strongest CIII] emitters in our sample, the redshift places the strong rest-optical lines in regions of poor atmospheric transmission. We have obtained multi-wavelength imaging in the optical and near-IR (Figure 4). The SED reveals a large sSFR (43.1 Gyr $^{-1}$), lit-

tle dust attenuation ($\hat{\tau}_V=0.53$), and a magnification-corrected stellar mass of $\log(M_\star/M_\odot) = 9.8$.

CSWA-139 was confirmed to have a redshift of $z = 2.54$ in Stark et al. (2013a) based on the presence of Ly α absorption and interstellar metal absorption lines in an MMT spectrum. The spectrum also shows emission from the [CIII],CIII] $\lambda\lambda 1907, 1909$ doublet with a total equivalent width of $W_{\text{CIII}} = 3.4 \pm 2.6 \text{ \AA}$. Here we present new optical and near-IR imaging from the LBT and MMT. The SED is best fit with an sSFR of 2.9 Gyr^{-1} , $\hat{\tau}_V=0.77$, and a stellar mass of $\log(M_\star/M_\odot) = 10.3$ after magnification correction.

CSWA-2 (SDSS J1038+4849) was first reported in Belokurov et al. (2009), and the source redshift ($z = 2.20$) was subsequently confirmed in Jones et al. (2013) through detection of rest-optical emission lines. The lens reconstruction described in Jones et al. (2013) shows that CSWA-2 is a merger of two systems with a stellar mass ratio $(6 \pm 3):1$. $\log(M_\star/M_\odot) = 9.1^{+0.2}_{-0.1}$ and one of the largest sSFR (19.9 Gyr^{-1}). The oxygen abundance $12+\log(\text{O/H})$ of the system as calculated by using N2 index is 8.25 ($\sim 0.4 Z_\odot$). The Balmer decrement ratio ($H\alpha/H\beta=3.47$) suggests little nebular extinction whereas O3 of 1.80 imply relatively larger excitation from ionized gas. Using the metallicity calibration of Bian et al. (2018), we estimate the oxygen abundance $12+\log(\text{O/H})$ of the system using the O3 index as 8.4 ($\sim 0.5 Z_\odot$). In this paper, we present new optical spectroscopy of this system obtained with ESI. The spectrum is dominated by continuum emission from the lower mass source (denoted J1038 North in Jones et al. (2013) which is considerably brighter in the optical. The spectrum shows emission from [CIII],CIII] $\lambda\lambda 1907, 1909$ with a total equivalent width of $W_{\text{CIII}}=3.1 \pm 1.8 \text{ \AA}$.

CSWA-39 (SDSS J1527+0652), a bright ($r = 20.5$) $z = 2.759$ galaxy was first identified as part of the SDSS Giant Arcs Survey (SGAS; Hennawi et al. 2008) and was spectroscopically confirmed by Koester et al. (2010) through detection of Ly α emission and interstellar absorption lines. We have obtained an ESI optical spectrum and multi-color optical imaging. Both components of the [CIII], CIII] doublet are detected in the spectrum, with a total S/N=16.1 for the summed doublet flux. The rest-frame equivalent width ($W_{\text{CIII}}=1.1 \text{ \AA}$) is typical of similarly luminous galaxies at this redshift (e.g., Shapley et al. 2003; Du et al. 2017). We also detect Ly α emission with a moderate rest-frame equivalent width ($W_{\text{Ly}\alpha}=11.8 \pm 6.2 \text{ \AA}$). No other nebular UV lines are detected in the ESI spectrum. The upper limit on the OIII] $\lambda\lambda 1661, 1666$ components imply equivalent widths below 1 \AA , consistent with the OIII] emission strengths in the Shapley et al. (2003) composite of $z \simeq 3$ galaxies with similar Ly α equivalent widths.

CSWA-38 (SDSS J1226+2152) was confirmed to lie at $z = 2.923$ by detection of Ly α and metal absorption lines in (Koester et al. 2010). Like CSWA-39, this source was first identified in Sloan Giant Arcs survey. Here we present deep ESI spectroscopy and imaging. The optical spectrum reveals a 4.1σ detection of the CIII] $\lambda 1909$ component, but the [CIII] $\lambda 1907$ component is situated on a skyline, precluding a useful limit. The rest-frame equivalent width of the CIII] $\lambda 1909$ component ($W_{\text{CIII}]\lambda 1909}=0.4 \text{ \AA}$) is comparable to CSWA-38 and CSWA-19. Ly α emission is weak ($W_{\text{Ly}\alpha}=0.4 \text{ \AA}$), and no other nebular UV lines are detected.

CSWA-19 (SDSS J0900+2234) was first confirmed in (Diehl et al. 2009) at $z = 2.03$ via detection of Ly α emission and several metal absorption features in a spectrum from the dual imaging spectrograph (DIS) on the Astrophysical Research Consortium (ARC) 3.5 meter telescope at the Apache Point Observatory. We have since obtained a deep ESI spectrum and MMT near-infrared imaging of

this source. The combined optical and near-infrared SED is best-fit by a model with a (magnification-corrected) stellar mass of $\log(M_\star/M_\odot) = 10.5$, a specific star formation rate of 0.5 Gyr^{-1} , and V-band attenuation optical depth of $\hat{\tau}_V=1.09$. The ESI spectrum of the source shows weak detections of [CIII], CIII] $\lambda\lambda 1907, 1909$ with an integrated S/N=8.6 across both components of the doublet. The total rest-frame equivalent width ($W_{\text{CIII}}=0.7 \text{ \AA}$) is among the lowest in our sample. No other nebular rest-UV lines are detected, as Ly α is situated to the blue of the ESI coverage.

CSWA-128 (SDSS J1958+5950) is a bright ($r=20.7$) $z=2.22$ galaxy that was spectroscopically confirmed in Stark et al. (2013a) through detection of rest-optical emission lines in an LBT/LUCI near-infrared spectrum and interstellar metal absorption lines in an MMT optical spectrum. We have since obtained optical and near-infrared imaging and a deep ESI optical spectrum. The magnification-corrected SED (Figure 4) implies a stellar mass of $\log(M_\star/M_\odot) = 9.9^{+0.3}_{-0.3}$ and an sSFR of 1.0 Gyr^{-1} . The ESI spectrum reveals a faint 4.8σ detection of [CIII], CIII] emission at the systemic redshift ($z = 2.225$) defined by the rest-optical lines, implying a rest-frame equivalent width of $W_{\text{CIII}}=0.7 \text{ \AA}$ for the doublet. No other nebular lines are detected in the rest-UV.

The flux ratios of rest-optical lines (Table 4) constrain the gas physical conditions, providing a framework to understand the weak UV nebular line emission. We infer the gas-phase oxygen abundance using the R23, O32 and O3 calibration presented in Bian et al. (2018). The three indices suggest metallicities of $12+\log \text{O/H} = 8.2$ (O32), $12+\log \text{O/H}=8.4$ (R23) and $12+\log \text{O/H}=8.5$ (O3). As discussed in Sanders et al. (2020), O32 metallicity calibration in Bian et al. (2018) may provide a better estimate of oxygen abundance for high redshift galaxy. This suggests that the metallicity of the ionized gas of CSWA-128 is $\sim 0.3\text{--}0.4 Z_\odot$. The values of O32 (3.3) and R23 (7.0) are a factor of 2.0 and 1.6 smaller than that of the strong CIII] emitter CSWA-141, consistent with expectations for nebular gas with a lower ionization parameter and excitation. In contrast, the electron density implied by the [SII] $\lambda\lambda 6717, 6731$ doublet (200 cm^{-3}) is similar to that found in both strong CIII] emitters such as CSWA-141 and typical $z \simeq 2\text{--}3$ galaxies (Sanders et al. 2016a).

CSWA-103 (SDSS J0145-0455) is a $z = 1.96$ galaxy that was confirmed in Stark et al. (2013a) through detection of metal absorption lines and weak Ly α emission in an MMT blue channel spectrum. We have since obtained a moderate resolution Keck/ESI spectrum and optical and near-infrared imaging with LBT and MMT, respectively. The broadband SED (Figure 4) is best fit by a stellar synthesis model with a stellar mass (magnification corrected) of $\log(M_\star/M_\odot) = 10.4$, sSFR= 0.7 Gyr^{-1} , and $\hat{\tau}_V=0.48$. The ESI spectrum constrains rest-frame wavelengths $1350\text{--}3425 \text{ \AA}$. Positive emission is detected from both components of the [CIII], CIII] doublet, implying a total rest-frame equivalent width of 0.5 \AA . No other nebular emission lines are observed in the ESI spectrum.

CSWA-164 (SDSS J0232-0323) was spectroscopically confirmed in Stark et al. (2013a) based on the presence of Ly α emission and interstellar absorption lines in an MMT blue channel spectrum. Stark et al. (2013a) also presented detection of [OII], [OIII] $\lambda 5007$, and H α in a Magellan/FIRE near-infrared spectrum of CSWA-164, revealing a systemic nebular redshift of $z = 2.512$. We have since obtained a deep moderate resolution optical spectrum with ESI and optical broadband imaging. The ESI spectrum reveals the Ly α emission ($W_{\text{Ly}\alpha} = 2.0 \text{ \AA}$) detected previously together with weak emission (S/N=4.1) from the [CIII], CIII] $\lambda\lambda 1907, 1909$ doublet. This corresponds to a total CIII], CIII] equivalent width of just 0.4 \AA , the smallest measured value in our sample.

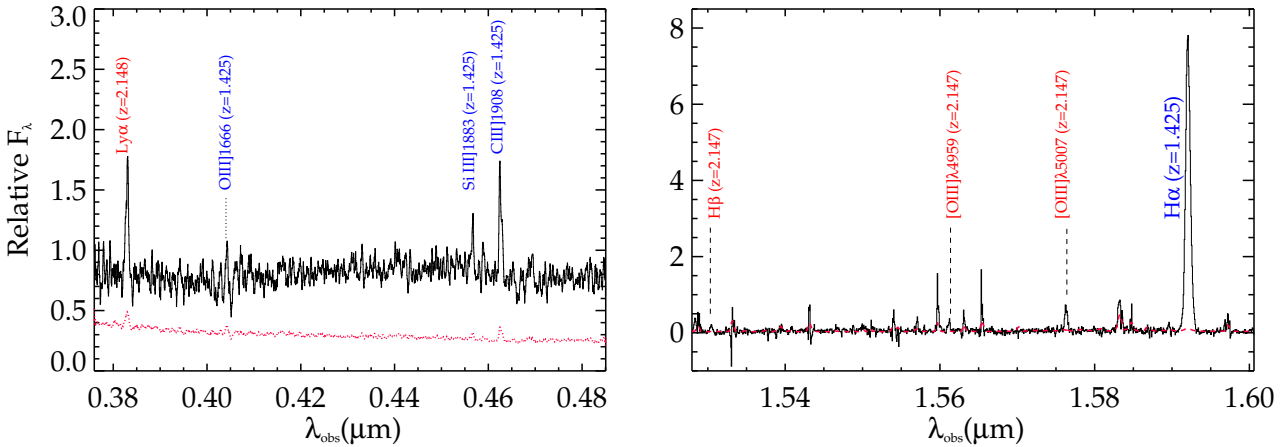


Figure 5. Optical and NIR spectra of CSWA-141. A secondary source (CSWA-141b) is identified in the Optical+NIR spectra (see §3) (Left:) Ly α emission at $z = 2.148$ from CSWA-141b in the LBT/MODS spectrum alongside [SiIII] $\lambda 1883$ and CIII] $\lambda 1908$ from CSWA-141 at $z = 1.425$. (Right:) Rest optical lines ([OIII] $\lambda\lambda 4959, 5007$, H β) from CSWA-141b at $z = 2.147$ observed in the FIRE spectrum alongside the H α emission line from CSWA-141.

The FIRE spectrum provides insight into the ionized gas physical conditions of CSWA-164. Unfortunately both H β and [NII] are obscured by skylines, precluding a robust determination of the oxygen abundance through standard strong line calibrations. We can however estimate oxygen abundance using O32 metallicity calibrations from [Bian et al. \(2018\)](#). We find that O32=0.7 corresponds to the oxygen abundance of 12+log O/H=8.6. Thus the ionized gas appear to be reasonably metal rich in CSWA-164. The value of ionization-sensitive line ratios (O32 = 0.7) is among the lowest in our sample. In contrast to the metallicity and ionization parameter, the electron density derived from the [OII] doublet (165 cm $^{-3}$) is consistent with the range spanned by other galaxies in our sample.

CSWA-40 (SDSS J0952+3434) is a $z = 2.190$ galaxy identified through the Sloan Bright Arcs Survey and spectroscopically confirmed by [Kubo et al. \(2010\)](#) using the DIS on the ARC 3.5 meter and the RC Spectrograph on the Mayall 4 meter telescope at Kitt Peak National Observatory. The spectra reveal Ly α in absorption along with several other metal absorption lines. We have obtained a moderate resolution optical spectrum and imaging with Keck/ESI. The continuum S/N of the CSWA-40 ESI spectrum is lower than other systems. This is the only ESI spectrum that does not reveal detection of the [CIII], CIII] doublet, implying a rest-frame equivalent width below 1.6 Å for the sum of both components. No other nebular emission lines are observed in the spectrum.

CSWA-163 (SDSS J2158+0257) was spectroscopically confirmed in [Stark et al. \(2013a\)](#) based on identification of metal absorption lines and Ly α absorption in an MMT blue channel spectrum. A Magellan/FIRE near-infrared spectrum was also obtained in that paper, revealing a systemic nebular redshift of $z = 2.079$ based on detection of [OII], H γ , H β , [OIII], H α , and [NII]. We have obtained new optical and near-infrared imaging of this source, allowing constraints to be placed on the broadband SED (Figure 4). The data are best fit by stellar synthesis models with stellar mass $\log(M_\star/M_\odot) = 9.9^{+0.1}_{-0.1}$ after magnification correction, V-band attenuation optical depth of $\hat{\tau}_V=0.67$, and an sSFR of 1.8 Gyr $^{-1}$, suggesting CSWA-163 is a relatively massive galaxy with a fairly evolved stellar population. Perhaps not surprisingly given the low sSFR and lack of Ly α emission, the MMT blue channel spectrum does not show any CIII] emission at the systemic redshift. The 3 σ

flux upper limit suggests that the rest-frame equivalent width of the doublet must be lower than 3.1 Å.

The FIRE spectrum provides useful constraints on the ionized gas of CSWA-163. The oxygen abundance can be derived from O32 and O3 calibration from [Bian et al. \(2018\)](#). Both suggest moderately enriched gas: 12+log O/H=8.5 (O32) and 12+log O/H=8.4 (O3) implying a nebular oxygen abundance of 0.4-0.5 Z $_\odot$. The ionization-sensitive line ratios (O32=1.1, O3=4.3) are consistent with a relatively low ionization parameter and moderate gas-excitation. The electron density inferred from [OII] is 144 cm $^{-3}$, consistent with the other systems studied in this paper.

CSWA-16 (SDSS J1111+5308) was confirmed to have a redshift of $z = 1.95$ based on the presence of numerous metal absorption lines in an MMT blue channel spectrum ([Stark et al. 2013a](#)). The discovery spectrum shows no emission from the blended [CIII], CIII] doublet. The 3 σ upper limit on the total flux from the doublet requires the rest-frame equivalent width to be smaller than 2.3 Å. We have obtained multi-band optical imaging with LBT, allowing more robust constraints to be placed on the apparent magnitude (r=21.8) and the magnification-corrected UV absolute magnitude (M_{UV}=−20.8).

CSWA-165 (SDSS J0105+0144) is a $z = 2.13$ galaxy that was first confirmed in [Stark et al. \(2013b\)](#) through detection of strong metal absorption lines and weak Ly α emission in an MMT blue channel spectrum. We have since obtained a Magellan/FIRE near-infrared spectrum and optical and near-infrared imaging from LBT and MMT respectively. The FIRE spectrum reveals detection of [OII], H β , [OIII] $\lambda 5007$, H α , and [NII], indicating a systemic redshift of $z = 2.128$. The MMT shows no emission from the [CIII], CIII] doublet at the systemic redshift. The 3 σ upper limit on the flux of the doublet indicates that the total CIII] equivalent width must be lower than 1.3 Å. The broadband SED is best-fit by a synthesis model with stellar mass of $\log(M_\star/M_\odot) = 10.0$, sSFR of 3.9 Gyr $^{-1}$, and $\hat{\tau}_V=0.62$.

The gas-phase metallicity can be inferred from O32, R23, and O3 strong line calibrations. All three indicate metal rich ionized gas: 12+log O/H = 8.4 (O32) 8.6 (R23), 8.6 (O3), consistent with a gas-phase metallicity in the range 0.5-0.8 Z $_\odot$. The ionization-sensitive ratios (O32=0.6, O3=2.1) suggest an ionization parameter that is lower than average among $z \simeq 2 - 3$ galaxies. In contrast,

the electron density derived from the [OII] doublet flux ratio (220 cm^{-3}) is similar to that found in other systems at high redshift.

CSWA-11 (SDSS J0800+0812) was confirmed at $z = 1.41$ via detection of metal absorption lines and [OII] emission in MMT blue and red channel spectra (Stark et al. 2013a). The CIII] doublet is not detected in either the blue or red channel MMT spectra, implying a rest-frame equivalent width below 0.9 \AA at 3σ . We have obtained multi-wavelength imaging and near-infrared spectroscopy. The magnification-corrected SED suggests a stellar mass of $\log(M_\star/M_\odot) = 10.0^{+0.4}_{-0.3}$, an sSFR of 7.4 Gyr^{-1} , and V-band attenuation optical depth of $\hat{\tau}_V = 0.28$. The FIRE spectrum reveals detections of [OII], [OIII] $\lambda 5007$, and $\text{H}\alpha$, but strong skylines obscure detections of $\text{H}\beta$, [OIII] $\lambda 4959$ and [NII] $\lambda 6586$. Using the theoretically-expected flux ratio of [OIII] $\lambda 5007$ /[OIII] $\lambda 4959$, we infer that this system has $\text{O32} = 0.92$, relatively low for our sample. Using the O32 calibration, we estimate metallicity of $12+\log \text{O/H} = 8.5$. The electron density implied by the [OII] doublet flux ratio is $469^{+416}_{-238} \text{ cm}^{-3}$, consistent with the range spanned by other galaxies in our sample.

CSWA-116 (SDSS J0143+1607) is a $z = 1.50$ galaxy confirmed in Stark et al. (2013a) through detection of rest-UV metal absorption lines and [OII] in MMT blue and red channel spectra. We do not detect the CIII] doublet in the MMT spectra, indicating that the rest-frame equivalent width is below 0.7 \AA at 3σ . We have obtained optical and near-infrared imaging of CSWA-116, providing constraints on the broadband SED. The data are best fit by a stellar model with $\log(M_\star/M_\odot) = 9.4$, an sSFR of 1.3 Gyr^{-1} , and V-band attenuation optical depth of $\hat{\tau}_V = 0.27$.

3.2 Physical Properties of CASSOWARY galaxy sample

The data obtained for this paper provide new constraints on the ionized gas properties and the stellar populations of lensed galaxies at $z \simeq 1 - 3$ identified by the CASSOWARY selection in SDSS. Here we briefly describe what these data reveal about the average properties in this sample, providing a concise summary of the source-by-source description presented in §3.1. Following correction for magnification, the rest-frame UV absolute magnitudes are found to range between $M_{\text{UV}} = -20.2$ and $M_{\text{UV}} = -23.0$, with a median value ($M_{\text{UV}} = -21.9$) that is roughly three times the value of L_{UV}^* at $z \simeq 2$ (e.g., Reddy & Steidel 2009). Both optical and near-infrared imaging exist for 11 of the 16 galaxies considered in this paper, allowing the stellar content to be characterized through SED fitting. The median stellar mass and sSFR of this subset is $1.3 \times 10^{10} M_\odot$ and 2.1 Gyr^{-1} , respectively. The latter is similar to the average sSFR of $z \simeq 2 - 3$ galaxies (e.g., Reddy & Steidel 2009).

Rest-optical line measurements exist for seven of the CASSOWARY galaxies shown in Figure 1. The median gas-phase oxygen abundance derived from the rest-optical line ratios is $12+\log \text{O/H} = 8.33$, i.e., ionized gas metallicity of $0.4 Z_\odot$. The ionization-sensitive ratio O32 ranges between 0.7 and 6.7 with a median value of $\text{O32} = 1.1$. While this is slightly lower than the median O32 in the KBSS and MOSDEF surveys, it is well within the range spanned by galaxies in these samples (e.g., Sanders et al. 2016a; Strom et al. 2016; Steidel et al. 2016). The Balmer decrements range between $\text{H}\alpha/\text{H}\beta = 3.47$ and 4.97. The median electron density derived from the [OII] or [SII] doublet flux ratios (198 cm^{-3}) is close to the average electron density of $z \simeq 2.3$ galaxies from the MOSDEF survey (Sanders et al. 2016a).

All sixteen galaxies in our sample have constraints on rest-UV line emission. Most sources show very weak [CIII], CIII] emission. The median equivalent width for the summed doublet is 1 \AA , similar

to that seen in composite spectra of $z \simeq 3$ LBGs (Shapley et al. 2003; Llerena et al. 2021). The two strongest [CIII], CIII] emitters (CSWA 141, CSWA -13) have rest-frame equivalent widths of 4.6 \AA and 4.4 \AA , respectively. The rest-UV spectrum of CSWA-141 also shows prominent nebular emission from OIII], Si III] and Mg II. While these lines are absent in CSWA-13, its spectrum does reveal broad He II emission, indicative of a significant Wolf Rayet population. No high ionization nebular lines are detected in our sample.

Our sample allows to compare and contrast ISM conditions expected in strong and weak CIII] emitters. A typical CIII] equivalent widths of star-forming galaxies at $z \sim 2 - 3$ is $\sim 1.7 \text{ \AA}$ (Shapley et al. 2003; Du et al. 2017). From here on, we refer to those galaxies with CIII] equivalent widths $> 2 \times$ typically seen at $z \sim 2 - 3$ ($\gtrsim 3.5 \text{ \AA}$) as strong CIII] emitters, whereas objects with CIII] equivalent widths below this threshold are described as weak CIII] emitters. Together with galaxies presented in this paper, we compile sources from the literature having constraints from both CIII] equivalent widths and optical spectra. The majority of the literature objects are lower redshifts galaxies (Giavalisco et al. 1996; Leitherer et al. 2011; Berg et al. 2016, 2019; Senchyna et al. 2017, 2019; Ravindranath et al. 2020), while majority of sample at $z > 1$ are comprised of gravitationally lensed systems (Mainali et al. 2020; de Barros et al. 2016; Stark et al. 2014; Vanzella et al. 2017; Berg et al. 2018; Bayliss et al. 2014; Vanzella et al. 2016; James et al. 2014; Erb et al. 2010; Christensen et al. 2012; Rigby et al. 2021; Quider et al. 2009; Hainline et al. 2009; Pettini et al. 2000; Teplitz et al. 2000; Jones et al. 2013). We present a compilation of $z > 1$ sources in Table 8.

In Figure 6, we plot empirical relationships between CIII] equivalent width and oxygen abundance (left panel), and CIII] equivalent width and O32 (right panel). The oxygen abundance of the strong CIII] emitters are mostly measured using direct metallicity measurements, while strong optical line calibrations are used for the weaker CIII] emitters (see Table 8). As can be seen in the Figure 6, the gas-phase metallicity of the strong CIII] emitters is consistently below $12+\log(\text{O/H}) = 8.0$, suggesting metallicities below $20\% Z_\odot$. In contrast, most of the weaker CIII] emitters imply higher metallicities than this value. This result is consistent with previous investigations in the literature (e.g., Rigby et al. 2015; Jaskot & Ravindranath 2016; Maseda et al. 2017; Nakajima et al. 2018; Schaerer et al. 2018; Senchyna et al. 2019; Ravindranath et al. 2020; Du et al. 2020; Tang et al. 2021). The right panel of Figure 6 shows that the O32 values of the stronger CIII] emitters ($\gtrsim 3.5 \text{ \AA}$) are on an average six times larger than the those of the weaker CIII] emitters. The median O32 value of the weaker CIII] emitters are similar to typical galaxies at $z \sim 2 - 3$ ($\text{O32} = 1.3$, Sanders et al. 2016a). A variety of factors can influence the O32 value of a galaxy. The elevated values seen in the strongest of CIII] emitters tend to be found in galaxies dominated by the light of a very young stellar population (Tang et al. 2021; Sanders et al. 2020), as expected in galaxies undergoing a burst of star formation. Overall these empirical relationships support a physical picture where galaxies with metal poor gas and young stellar populations are able to power strong CIII] emission (e.g. Stark et al. 2014; Rigby et al. 2015; Senchyna et al. 2017). The scatter seen in the CIII] EW at a given metallicity or O32 value may stem from differences in ISM conditions (relative carbon abundances (C/O), ionization parameters) and stellar age and metallicity.

The compilation of strong CIII] emitters further provides information on the global spectral properties expected from typical reionization era systems. In Figure 7, we show strong CIII] emitters (denoted by red square) and weak CIII] emitters (denoted by blue square) in $\log(\text{[OIII]}/\text{H}\beta)$ vs sSFR (left panel) and $\log(\text{O32})$

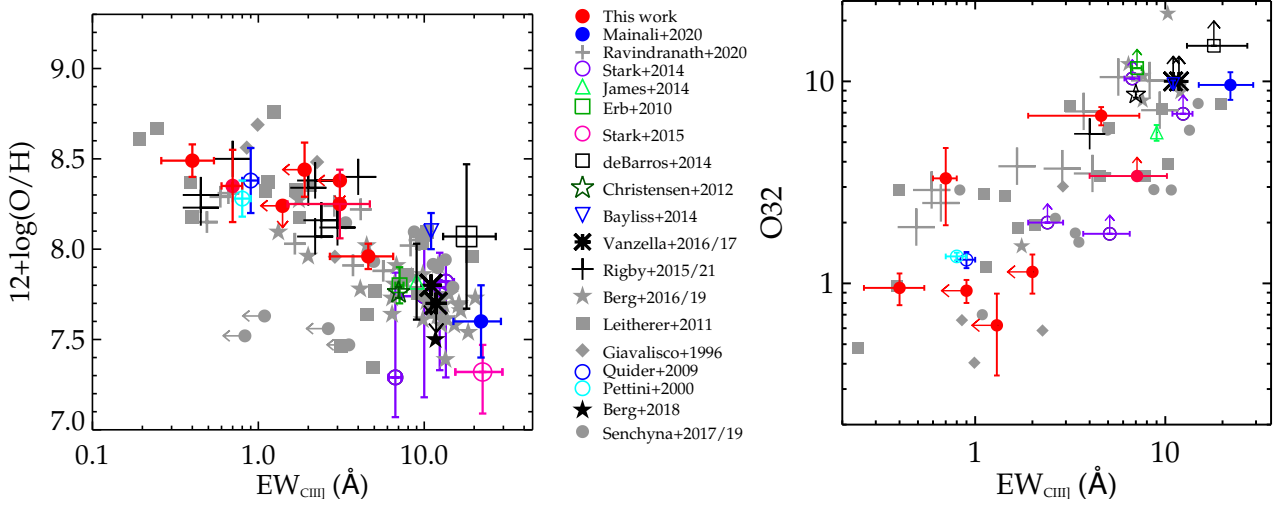


Figure 6. (Left:) Empirical relationship between oxygen abundance ($12+\log(\text{O/H})$) and rest frame CIII] equivalent width (EW_{CIII}). (Right:) Empirical relationship between the line ratio of $[\text{OIII}]\lambda\lambda 4959,5007$ to $[\text{OII}]\lambda\lambda 3727,3729$ (i.e. O32) and rest-frame CIII] EW (EW_{CIII}). The red symbol represents bright lensed galaxies presented in this paper, while other data points are compilation from the literature.

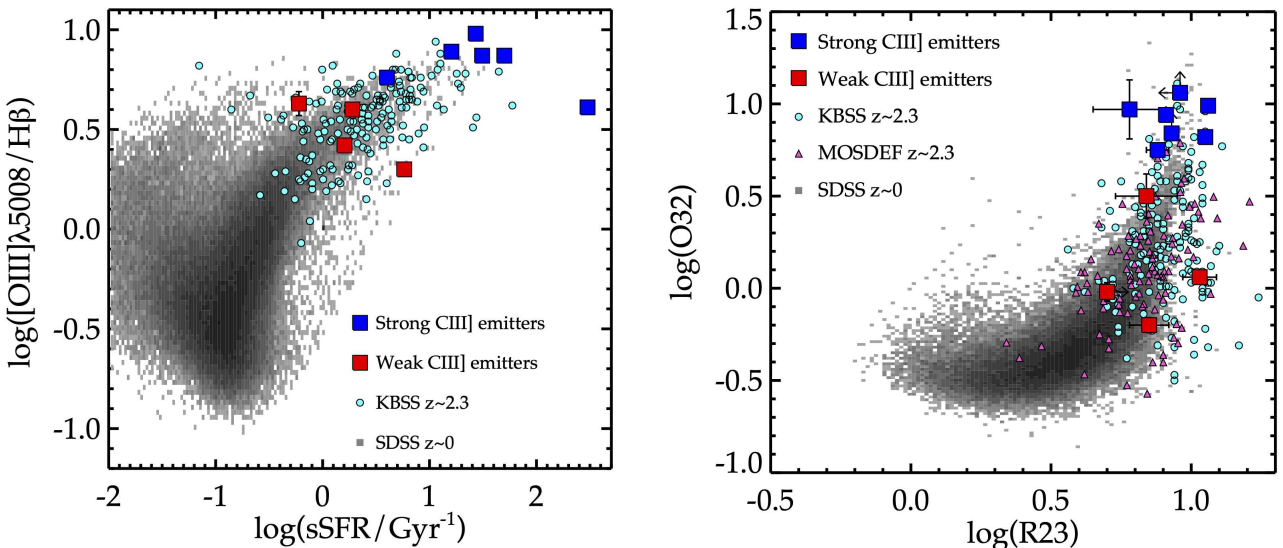


Figure 7. The strong (blue) and weak (red) CIII] emitters (see §3.2) in O3 vs sSFR (left) and O32 vs R23 (right) plots. Star forming galaxies at $z \sim 2.3$ from KBSS survey (Strom et al. 2016) are shown in cyan circle whereas MOSDEF survey (Sanders et al. 2016a) are shown in violet triangle. Local galaxies from SDSS survey are shown in grey. Galaxies with properties similar to those at $z > 6$ tend to have strongest C III] emission.

vs $\log(\text{R23})$ (right panel) plots. We compare them to typical line ratios expected at $z \sim 2$ using dataset from KBSS survey (Steidel et al. 2014; Strom et al. 2016) and MOSDEF survey (Sanders et al. 2016a), as well as at $z \sim 0$ (local SDSS galaxies). The strong CIII] emitting galaxies appears to be distinct from local SDSS galaxies as well as typical galaxies at $z \sim 2$ in both the plots. However, the position of weaker CIII] emitters on both the diagrams is similar to typical galaxies at $z \sim 2$. Taken together, this further demonstrates that strong CIII] emitters show highly ionized gas conditions from a large sSFR systems. Assuming these strong CIII] emitters representative of a typical reionization era systems, we might expect a similar ISM conditions in galaxies at $z > 6$.

4 DISCUSSION

In this paper, we present spectra of some of the brightest-known gravitationally-lensed galaxies at $z \simeq 2-3$, discovered over the footprint of SDSS. Included in this sample are CSWA-13 and CSWA-141, two exceptionally bright systems with sSFRs ($> 20 \text{ Gyr}^{-1}$) that are similar to those of the reionization-era. Their spectra reveal rest-frame CIII] equivalent widths more than twice what is typical at $z \simeq 2-3$ (e.g., Shapley et al. 2003; Du et al. 2018; Llerena et al. 2021). In this section, we explore the ionized gas conditions and the properties of the outflowing gas, taking advantage of emission and absorption lines that are often too faint to be detected in individual high redshift galaxies with similarly intense emission lines.

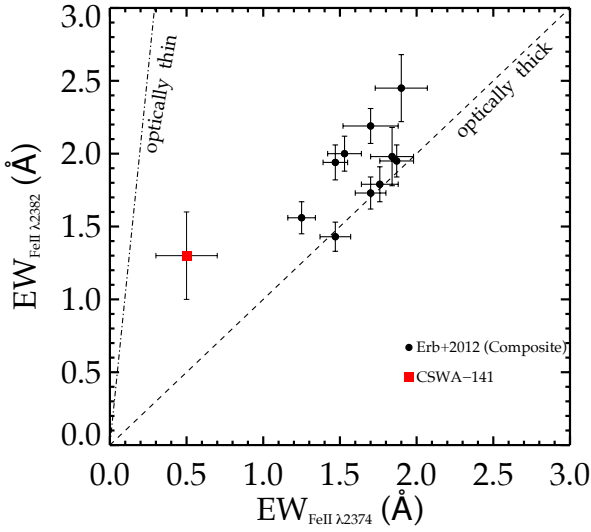


Figure 8. A comparison between equivalent widths of Fe II $\lambda 2374$ and Fe II $\lambda 2382$. The red square represents CSWA-141 data point whereas black circles are composite data points presented in Erb et al. 2012. The two dashed black lines represent optically thin and optically thick cases. This reflects that Fe II is not optically thick in CSWA-141 and therefore has a lower column density c.f. black points

Our analysis will primarily focus on CSWA-141, as the redshift of CSWA-13 places the strong rest-optical lines in regions of low atmospheric transmission. For CSWA 141, the rest-optical lines are similar in equivalent width to those found in the reionization era (e.g., De Barros et al. 2017; Endsley et al. 2020; Boyett et al. 2022), classifying this galaxy as an EELG and revealing a stellar population dominated by a recent burst or upturn in star formation.

The gas properties in such intense line emitting galaxies have been the subject of a number of spectroscopic investigations in recent years. These studies demonstrate that the nebular gas is generally under extreme ionization conditions in EELGs (Tang et al. 2018), with the ionization parameter reaching its largest values in the galaxies powered by the youngest stellar populations (or the largest equivalent width rest-optical nebular lines). The gas in CSWA-141 is consistent with this picture, showing a large O32 ratio (6.7) as expected given its elevated sSFR (31.2 Gyr^{-1}) and [OIII]+H β EW (730 Å). Its large ionization parameter implied by the photoion-isaiton models ($\log U = -2.1$) suggests a large photon density is impinging on the ionised gas. This can be driven by a variety of factors, including efficient ionizing photon production (e.g., Chevallard et al. 2018; Tang et al. 2021) and a compact configuration of ionized gas around the sources of ionizing radiation. The latter is the norm for galaxies dominated by very young stellar clusters (e.g., Whitmore et al. 2011; Hannon et al. 2019; Chen et al. 2023), and thus may be expected in EELGs like CSWA-141.

Further insight into the gas conditions of EELGs is made possible by detection of three density-sensitive emission lines in CSWA-141. As we discussed in §3.1, the [CIII], CIII] doublet implies very high gas densities ($16500^{+12100}_{-7800} \text{ cm}^{-3}$), perhaps again reflecting a very compact or concentrated gas geometry surrounding the extremely young star clusters that power EELGs. Although the uncertainty in CIII] density is currently large, such high densities are routinely seen in $z \approx 2 - 4$ galaxies with spectrally-resolved CIII] measurements (e.g., Christensen et al. 2012; James et al. 2014, 2018;

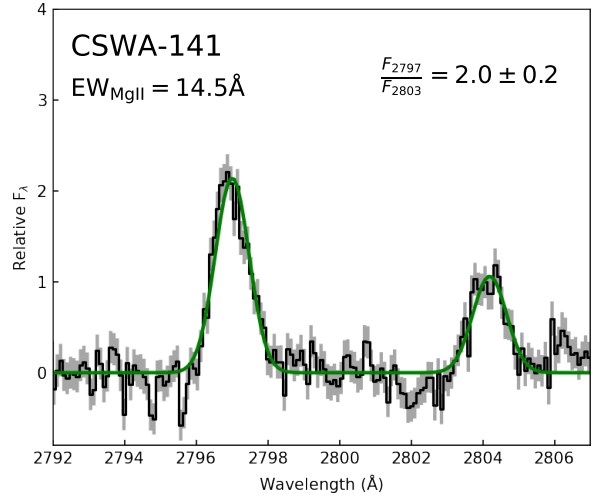


Figure 9. Mg II 2797,2803 line profile in CSWA-141. The black curve represents continuum subtracted flux level while the green solid line is gaussian fit to the observed data. Both the Mg II doublet are well fitted by a single component gaussian. Mg II 2797 is clearly stronger than Mg II 2803 line, suggesting a Mg II doublet intensity ratio (F_{2797}/F_{2803}) of 2.0 ± 0.2 . The doublet ratio is consistent with the intrinsic recombination value (2.0) indicating minimal scattering by low-ionization ISM along the line of sight. Based on the observed Mg II doublet ratio, CSWA-141 has implied escape fraction of $f_{\text{esc}}(\text{LyC}) = 27 \pm 4\%$.

Bayliss et al. 2014; Acharyya et al. 2019) and are also starting to be seen in the first handful of $z \gtrsim 7$ galaxies with CIII] doublet measurements (Stark et al. 2017; Jiang et al. 2021). As such, the high C III] density is less likely due to a statistical fluctuation, although a larger sample should confirm this. In most of the cases, the CIII] density is also significantly in excess of that inferred from lower-ionization species. The same trend is apparent in CSWA-141, with the CIII] density being nearly two orders of magnitude higher than those derived from [SII] and [OII]. This is consistent with a picture (e.g., Kewley et al. 2019; Acharyya et al. 2019; Berg et al. 2021) dictated by the ionization structure of the nebulae, with the lower ionization rest-optical lines (i.e., [OII] and [SII]) probing primarily the outer layers which are preferentially dominated by lower density gas. The higher ionization lines (like CIII]) probe the inner regions of the nebula, where densities are expected to be higher. Variations in the critical density of the ions will additionally contribute to CIII] probing higher density gas than [OII] (e.g., James et al. 2018). A key question is whether very young EELGs like CSWA-141 (and many of the $z > 7$ galaxies) might have a large fraction of their ionized gas in very dense clumps, as is expected at the earliest evolutionary phases following the formation of star clusters (e.g., Kim et al. 2018; Rigby & Rieke 2004). Currently samples with CIII] densities tend to be those that have at least moderately large CIII] EW, generally indicative of a relatively young stellar population. Larger CIII] density samples are required to test whether the presence of very large densities is at all sensitive to the luminosity-weighted stellar population age.

CSWA 141 also provides a unique window on the kinematics and covering fraction of the outflowing gas in EELGs, a population which becomes commonplace at $z > 6$. As it is this outflowing gas which regulates the escape of ionising radiation, systems like

CSWA 141 offer potential for understanding the likely contribution of EELGs to reionisation. At low redshift, (Jaskot et al. 2017; Chisholm et al. 2017) find that the most extreme [OIII] emitting galaxies (the Green Peas) tend to have low outflow velocities and suggest that this is consistent with models of suppressed superwinds, where catastrophic cooling prevents the development of large scale outflows (e.g., Silich et al. 2007; Silich & Tenorio-Tagle 2017; Gray et al. 2019). The low ionization absorption lines in the CSWA 141 spectra are all blueshifted with respect to the systemic redshift, indicating the presence of outflows. In the ESI spectrum, we detect Fe II and Mg II absorption lines, while the MODS spectrum probes slightly bluer wavelengths, allowing detection of Al II λ 1670. The average velocity of low ionization outflowing gas in CSWA 141 is 76 km s $^{-1}$. This is slightly lower than outflow velocities of 100-300 km s $^{-1}$ that are commonly observed in galaxies at $z \sim 1 - 3$ (e.g., Shapley et al. 2003; Weiner et al. 2009; Steidel et al. 2010; Jones et al. 2012). However given the low stellar mass of CSWA-141, the measurement is consistent with expectations from known trends between galaxy mass and outflow velocity (e.g., Martin 2005; Weiner et al. 2009; Erb et al. 2012; Chisholm et al. 2016).

The strength of the absorption lines in CSWA 141 provide insight into the opacity of neutral gas along the line of sight to the young star clusters which dominate the light. The Fe II λ 2374 and Fe II λ 2382 absorption lines are very weak with equivalent widths of 0.5 Å and 1.5 Å, respectively. Jones et al. (2018) measured a column density $N(\text{Fe II}) = 1.5^{+0.7}_{-0.2} \times 10^{14} \text{ cm}^{-2}$, which is among the lowest of the sample. In Figure 8, we compare these equivalent widths with those measured from composite spectra of more typical star forming galaxies at $1 < z < 2$ (Erb et al. 2012). As is clear in the figure, most star forming galaxies at these redshifts show similar Fe II λ 2374 and Fe II λ 2382 equivalent widths, as expected for optically thick neutral gas. In contrast, the Fe II λ 2374 absorption in CSWA-141 is significantly weaker than Fe II λ 2382. With an Fe II λ 2374 EW that is roughly three times weaker than that found in the $z \approx 1 - 2$ composites, the lines are much closer to expectations for optically thin neutral gas. We additionally note that the Fe II λ 2382 line is susceptible to emission filling (e.g., Erb et al. 2012) which tends to weaken the observed Fe II λ 2382 equivalent widths. This is particularly likely to be the case for EELGs like CSWA-141. In such a scenario, the line ratio would move even closer to that expected for optically thin conditions, implying a low covering fraction and potentially low column density of neutral gas in the outflow.

Further indications that CSWA 141 has a low column density of neutral gas comes from the resonant Mg II $\lambda\lambda$ 2797,2803 emission line. Both components of the doublet are confidently detected ($S/N > 10$) in emission with total equivalent widths of 14.5 Å (Figure 9). This is not only one of the highest measured Mg II EWs at $z > 1$, but it is also one of the brightest Mg II emission lines, making detailed (and resolved) study of the line uniquely possible. Recent studies have pointed out that the flux ratio of the doublet is strongly sensitive to the neutral gas column density in the galaxy. As such it is thought to correlate closely with the ionizing photon escape fraction (Henry et al. 2018; Chisholm et al. 2020; Xu et al. 2022; Seive et al. 2022; Xu et al. 2023), perhaps providing one of the best indirect indicators of photon leakage. At low HI column densities ($< 10^{17.2} \text{ cm}^{-2}$), galaxies become optically thin to the resonant Mg II line photons (Chisholm et al. 2020). This leads to strong nebular Mg II emission, and it drives the doublet ratio ($R = F_{2797}/F_{2803}$) to its intrinsic value of $R = 2$. If the line photons are resonantly scattered by Mg $^{+}$ ions in the neutral gas along the line of sight, the doublet ratio will decrease, asymptotting to a value of $R=1$ if the gas

is optically thick to Mg II photons (see Chisholm et al. 2020 for a detailed discussion).

The measured Mg II doublet ratio in CSWA-141 is $R=2.0 \pm 0.2$, consistent with the intrinsic value produced in the HII regions. This suggests that optically thin channels along the line of sight to the young star clusters are powering the nebular emission. Both components of the doublet are well-fit by single Gaussians, suggesting that the line profile is not significantly impacted by resonant scattering. The very large EW of the line also points to minimal attenuation of line photons. We note that the Mg II profile does show very weak blue-shifted absorption (see Figure 9), suggesting the presence of some neutral gas along the line of sight, but this gas must be either optically thin or clumpy with low density channels to result in the observed line profile.

Given the derived oxygen abundance of CSWA-141 (see §3.1) and nominal assumptions on the Mg/O ratio (Chisholm et al. 2020), this can be converted to an estimate of the hydrogen column density (See equation 14 of Chisholm et al. 2020). Given the measured doublet ratio is consistent with the intrinsic value, CSWA-141 is formally consistent with a negligible hydrogen column density. Within the measurement errors of the flux ratio, we find a 1σ upper limit on the HI column density of $3.8 \times 10^{16} \text{ cm}^{-2}$. This value is well below the HI column density at which galaxies become optically thin to LyC radiation ($< 10^{17.2} \text{ cm}^{-2}$), suggesting that CSWA-141 may be a likely candidate for LyC leakage. While more realistic geometries (i.e., clumpy gas) would alter the derived column densities, the observed line profile requires there to be low density channels along the line of sight where resonant line photons (and potentially LyC emission) are transmitted (Gazagnes et al. 2020; Saldana-Lopez et al. 2022). Because of the extreme brightness of CSWA-141, it presents a unique opportunity to spatially resolve the absorbing gas in an extreme line emitter that is very similar in its properties to those systems at $z > 6$. An upcoming *HST* UVIS grism observations (GO-16710, PI: Mainali) will provide more direct constraints on the escape of ionizing radiation from the galaxy.

5 SUMMARY

We present new spectroscopic and photometric observations of sixteen bright gravitationally lensed galaxies originally identified in SDSS via the CASSOWARY program. Observations were conducted using LBT, Keck, MMT and Magellan. Included in this sample is the $z = 1.42$ galaxy CSWA-141, one of the brightest known EELGs at high redshift, with an [OIII]+H β EW (730 Å) nearly identical to the average value seen at $z \approx 7 - 8$. In this paper, we focus on the rest-UV spectral properties of the sample, leveraging high quality Keck/ESI data. Owing to the brightness of our targets ($g \approx 19-21$), we are able to detect rest-UV metal line emission in the Keck spectra down to very low EW values. While most systems have weak line emission (median CIII] EW = 1.7 Å), CSWA 141 shows relatively strong emission (CIII] EW 4.6 Å) together with detections of a variety of UV lines (OIII], Si III], Fe II*, Mg II).

We compare the properties of the strong ($\gtrsim 3.5$ Å) and weak ($\lesssim 3.5$ Å) CIII] emitters in our sample and in the literature. We find that the stronger CIII] emitters have larger sSFR and lower gas-phase oxygen abundances. We find that the strong CIII] emitters can be easily separated by their rest-optical line ratios, with larger values of O32 at roughly fixed R23. Overall, these results suggest that CIII] tends to be strong in galaxies dominated by young stellar populations with low metallicity and extreme ionization conditions.

Object	EW _{CIII]} (\AA)	R23	O32	O3	Electron Density (cm^{-3})	12 + log (O/H)	Reference
CSWA-141	4.6 \pm 1.9	11.4 \pm 1.0	6.6 \pm 1.0	7.4 \pm 0.2	160 $^{+76a}_{-74}$, 350 $^{+294b}_{-206}$, 16500 $^{+12100c}_{-7800}$	7.95 \pm 0.08 ^d	This work
CSWA-2	3.1 \pm 1.6	5.2 \pm 2.1	...	8.4 \pm 0.2 ^g	This work, 16
CSWA-128	0.7 \pm 0.1	7.0 \pm 1.2	3.3 \pm 0.8	4.0 \pm 1.1	198 $^{+85b}_{-76}$	8.2 \pm 0.2 ^e , 8.4 \pm 0.2 ^f , 8.5 \pm 0.2 ^g	This work
CSWA-164	0.4 \pm 0.1	...	0.7 \pm 0.2	...	165 $^{+65a}_{-46}$	8.6 \pm 0.2 ^e	This work
CSWA-163	< 3.1	10.9 \pm 1.1	1.1 \pm 0.1	4.3 \pm 0.6	144 $^{+45a}_{-33}$	8.5 \pm 0.2 ^e , 8.4 \pm 0.2 ^g	This work
CSWA-165	< 1.9	7.1 \pm 1.3	0.6 \pm 0.1	2.1 \pm 0.4	221 $^{+75a}_{-64}$	8.4 \pm 0.2 ^e , 8.6 \pm 0.2 ^f , 8.6 \pm 0.2 ^g	This work
CSWA-11	< 1.4	...	0.8 \pm 0.2	...	469 $^{+120a}_{-156}$	8.5 \pm 0.2 ^e	This work
RXCJ0232-588	21.7	6.0	9.4	4.1	80 ^a	7.61 ^d	1
Ion2	18	...	> 15	14.7	...	8.07 ^h	2
860_359	12.4	< 9.2	> 6.91	6.0	...	< 8.1 ^f	3
ID14	11.8	< 11.7	> 10	7.6	...	< 7.8 ^d	4
SL2S0217	11.7	3.1	300 ^c	7.5 ^d	5
SGAS J1050+0017	11	11.4	9.7	7.9	2-3 \times 100 ^a	> 8.1 ^d	6
ID11	11	< 11.8	> 10	8.4	...	7.7 ^d	7
CSWA-20	9.1	7.7	5.6	4.9	276 ^a , 17100 ^b	7.82 ^d	8
BX418	7.1	< 9.2	> 11.6	6.4	...	7.8 ^d	9
A1689 31.1	7	7.8	8.2	4.7	330 ^a , 2900 ^c	7.76 ^d	10
MACS 0451-1.1	6.7	< 5.9	> 8.4	3.9	...	< 8.0 ^f	3
SDSS J1723+3411	4.0	8.6	5.5	5.4	47 ^a , 1950 ^c	8.4 ^f	11
MACS 0451-3.1	2.4	...	> 2.0	3
Cosmic Horseshoe	0.9	5.5	1.31	2.4	840-6900 ^b	8.65 ^f	12,13
MS 1512-cB58	0.8	7.9	1.36	3.6	...	8.47 ^f	14,15

^aDerived from [OII] doublet, ^bDerived from [SII] doublet, ^cDerived from CIII] doublet.

^dDirect (T_e) method, ^eO32 method, ^fR23 method, ^gO3 method,

^h Using HII-CHI-mistry code (Perez-Montero 2014)

¹Mainali et al. (2020), ²de Barros et al. (2016), ³Stark et al. (2014), ⁴Vanzella et al. (2017), ⁵Berg et al. (2018), ⁶Bayliss et al. (2014), ⁷Vanzella et al. (2016), ⁸James et al. (2014), ⁹Erb et al. (2010), ¹⁰Christensen et al. (2012), ¹¹Rigby et al. (2021), ¹²Quider et al. (2009), ¹³Hainline et al. (2009), ¹⁴Pettini et al. (2000), ¹⁵Teplitz et al. (2000), ¹⁶Jones et al. (2013)

Table 8. Rest-optical emission line properties of galaxies at high redshift with CIII] emission constraints. The upper half shows data from this paper whereas lower half shows measurements from the literature.

This is consistent with trends found in observations at low and high redshift (e.g., Rigby et al. 2015; Senchyna et al. 2017, 2019; Maseda et al. 2017; Nakajima et al. 2018; Schaefer et al. 2018; Du et al. 2020; Ravindranath et al. 2020; Tang et al. 2021) and in photoionization models (e.g., Jaskot & Ravindranath 2016; Nakajima et al. 2018).

The brightness of CSWA-141 enables a detailed investigation of an EELG with properties similar to that which become common at $z > 6$. This galaxy is characterized by low stellar mass ($4.0 \times 10^8 M_\odot$), large sSFR (31.2 Gyr $^{-1}$), low gas-phase metallicity (12+log O/H=7.95) and relatively highly ionized gas (O32=6.7) and has likely undergone a recent upturn or burst of star formation. We find that the electron density traced by the CIII] doublet ($1.65 \times 10^4 \text{ cm}^{-3}$) is higher than that traced by [OII] and [SII] doublet (160 and 350 cm^{-3} , respectively), a discrepancy that is also found in other systems (e.g., James et al. 2014; Acharyya et al. 2019). While this is likely to reflect the ionization structure of the HII regions powering the lines (Kewley et al. 2019), it may also indicate that CSWA-141 contains a significant fraction of its ionized gas in very dense clumps, as is expected in the earliest stages following the formation of star clusters (e.g. Kim et al. 2018).

The spectra of CSWA-141 provide several probes of the neutral gas opacity in the galaxy, including both low ionization absorption lines and the resolved Mg II doublet. The Fe II $\lambda\lambda$ 2374, 2382 absorption lines indicate the presence of outflowing gas with average velocity of 76 km s^{-1} . The lines are much weaker than in typical star forming galaxies at $z \approx 1 - 2$, implying a low covering fraction and potentially low column density of neutral gas in the outflow. The res-

onant Mg II $\lambda\lambda$ 2797,2803 emission line supports this picture. The Mg II doublet ratio in CSWA-141 ($R = F_{2797}/F_{2803}$) is 2.0 ± 0.2 , consistent with the intrinsic value produced in the HII regions. When combined with the very large EW of Mg II and the near-Gaussian profiles of the doublet components, this suggests minimal resonant scattering, consistent with a very low column density of neutral hydrogen. These indirect indicators suggest CSWA-141 may be a likely candidate for LyC leakage.

ACKNOWLEDGMENTS

We would like to thank Ryan Endsley for helping with MMT observations of some of the sources presented in this paper. We also thank Stephane Charlot and Jacopo Charlot for making the BEAGLE population synthesis tool available to us for this paper.

DPS acknowledges support from the National Science Foundation through the grant AST-2109066. TJ acknowledges support from the National Science Foundation through the grant AST-2108515. RSE acknowledges funding from the European Research Council (ERC) under the European Union’s Horizon 2020 research and innovation programme (grant agreement No 669253). Y.H. acknowledges support from the National Sciences and Engineering Council of Canada grant RGPIN-2020-05102, the Fonds de recherche du Québec grant 2022-NC-301305, and the Canada Research Chairs Program.

Observations presented in this paper were obtained from the

Keck Observatory, which was made possible by the generous financial support of the W. M. Keck Foundation. The material is based upon work supported by NASA under award number 80GSFC21M0002. The authors acknowledge the very significant cultural role that the summit of Mauna Kea has always had within the indigenous Hawaiian community. We are most fortunate to have the opportunity to conduct observations from this mountain. Some of the observations reported here were obtained at the MMT Observatory, a joint facility of the University of Arizona and the Smithsonian Institution. This paper includes data gathered with the 6.5 meter Magellan Telescopes located at Las Campanas Observatory, Chile. Some of the data presented in this paper were obtained using the Large Binocular Telescope (LBT). The LBT is an international collaboration among institutions in the United States, Italy and Germany. The LBT Corporation partners are: The University of Arizona on behalf of the Arizona university system; Istituto Nazionale di Astrofisica, Italy; LBT Beteiligungsgesellschaft, Germany, representing the Max Planck Society, the Astrophysical Institute Potsdam, and Heidelberg University; The Ohio State University; The Research Corporation, on behalf of The University of Notre Dame, University of Minnesota and University of Virginia.

DATA AVAILABILITY

The data underlying this article will be shared on reasonable request to the corresponding author.

REFERENCES

Acharyya A., et al., 2019, *MNRAS*, **488**, 5862

Bayliss M. B., Rigby J. R., Sharon K., Wuyts E., Florian M., Gladders M. D., Johnson T., Oguri M., 2014, *ApJ*, **790**, 144

Belokurov V., et al., 2007, *ApJ*, **671**, L9

Belokurov V., Evans N. W., Hewett P. C., Moiseev A., McMahon R. G., Sanchez S. F., King L. J., 2009, *MNRAS*, **392**, 104

Berg D. A., Skillman E. D., Henry R. B. C., Erb D. K., Carigi L., 2016, *ApJ*, **827**, 126

Berg D. A., Erb D. K., Auger M. W., Pettini M., Brammer G. B., 2018, *ApJ*, **859**, 164

Berg D. A., Erb D. K., Henry R. B. C., Skillman E. D., McQuinn K. B. W., 2019, *ApJ*, **874**, 93

Berg D. A., Chisholm J., Erb D. K., Skillman E. D., Pogge R. W., Olivier G. M., 2021, *ApJ*, **922**, 170

Berg D. A., et al., 2022, *ApJS*, **261**, 31

Bian F., et al., 2010, *ApJ*, **725**, 1877

Bian F., Kewley L. J., Dopita M. A., 2018, *ApJ*, **859**, 175

Bouwens R. J., et al., 2014, *ApJ*, **793**, 115

Bouwens R. J., et al., 2015, *ApJ*, **803**, 34

Bouwens R. J., et al., 2021, *AJ*, **162**, 47

Boyett K. N. K., Stark D. P., Bunker A. J., Tang M., Maseda M. V., 2022, *MNRAS*, **513**, 4451

Bruzual G., Charlot S., 2003, *MNRAS*, **344**, 1000

Calzetti D., Armus L., Bohlin R. C., Kinney A. L., Koornneef J., Storchi-Bergmann T., 2000, *ApJ*, **533**, 682

Chabrier G., 2003, *PASP*, **115**, 763

Chen Z., Stark D. P., Endsley R., Topping M., Whitler L., Charlot S., 2023, *MNRAS*, **518**, 5607

Chouvellard J., Charlot S., 2016, *MNRAS*, **462**, 1415

Chouvellard J., et al., 2018, *MNRAS*, **480**, 2593

Chisholm J., Tremonti C. A., Leitherer C., Chen Y., Wofford A., 2016, *MNRAS*, **457**, 3133

Chisholm J., Orlitová I., Schaefer D., Verhamme A., Worseck G., Izotov Y. I., Thuan T. X., Guseva N. G., 2017, *A&A*, **605**, A67

Chisholm J., Prochaska J. X., Schaefer D., Gazagnes S., Henry A., 2020, *MNRAS*, **498**, 2554

Christensen L., et al., 2012, *MNRAS*, **427**, 1953

Curtis-Lake E., et al., 2016, *MNRAS*, **457**, 440

De Barros S., et al., 2017, *A&A*, **608**, A123

Diehl H. T., et al., 2009, *ApJ*, **707**, 686

Du X., Shapley A. E., Martin C. L., Coil A. L., 2017, *ApJ*, **838**, 63

Du X., et al., 2018, preprint, ([arXiv:1803.05912](https://arxiv.org/abs/1803.05912))

Du X., Shapley A. E., Tang M., Stark D. P., Martin C. L., Mobasher B., Topping M. W., Chevallard J., 2020, *ApJ*, **890**, 65

Endsley R., Stark D. P., Chevallard J., Charlot S., 2020, *MNRAS*, **498**, 2554

Erb D. K., Pettini M., Shapley A. E., Steidel C. C., Law D. R., Reddy N. A., 2010, *ApJ*, **719**, 1168

Erb D. K., Quider A. M., Henry A. L., Martin C. L., 2012, *ApJ*, **759**, 26

Ferland G. J., et al., 2013, *Rev. Mex. Astron. Astrofis.*, **49**, 137

Finkelstein S. L., et al., 2014, Submitted to *ApJ*, arxiv:1410.5439,

Gazagnes S., Chisholm J., Schaefer D., Verhamme A., Izotov Y., 2020, *A&A*, **639**, A85

Giavalisco M., Koratkar A., Calzetti D., 1996, *ApJ*, **466**, 831

González V., Bouwens R., Illingworth G., Labbé I., Oesch P., Franx M., Magee D., 2014, *ApJ*, **781**, 34

Gray W. J., Oey M. S., Silich S., Scannapieco E., 2019, *ApJ*, **887**, 161

Grazian A., et al., 2015, *A&A*, **575**, A96

Guseva N. G., Izotov Y. I., Fricke K. J., Henkel C., 2019, *A&A*, **624**, A21

Gutkin J., Charlot S., Bruzual G., 2016, *MNRAS*, **462**, 1757

Hainline K. N., Shapley A. E., Kornei K. A., Pettini M., Buckley-Geer E., Allam S. S., Tucker D. L., 2009, *ApJ*, **701**, 52

Hannan S., et al., 2019, *MNRAS*, **490**, 4648

Hennawi J. F., et al., 2008, *AJ*, **135**, 664

Henry A., Berg D. A., Scarlata C., Verhamme A., Erb D., 2018, *ApJ*, **855**, 96

Hezaveh Y. D., et al., 2013, *ApJ*, **767**, 132

Hutchison T. A., et al., 2019, arXiv e-prints, [p. arXiv:1905.08812](https://arxiv.org/abs/1905.08812)

Ishigaki M., Kawamata R., Ouchi M., Oguri M., Shimasaku K., Ono Y., 2018, *ApJ*, **854**, 73

Izotov Y. I., Stasińska G., Meynet G., Guseva N. G., Thuan T. X., 2006, *A&A*, **448**, 955

Izotov Y. I., Chisholm J., Worseck G., Guseva N. G., Schaefer D., Prochaska J. X., 2022, *MNRAS*, **515**, 2864

James B. L., et al., 2014, *MNRAS*, **440**, 1794

James B. L., Auger M., Pettini M., Stark D. P., Belokurov V., Carniani S., 2018, *MNRAS*, **476**, 1726

Jaskot A. E., Ravindranath S., 2016, *ApJ*, **833**, 136

Jaskot A. E., Oey M. S., Scarlata C., Dowd T., 2017, *ApJ*, **851**, L9

Jiang L., et al., 2021, *Nature Astronomy*, **5**, 256

Jones T., Stark D. P., Ellis R. S., 2012, *ApJ*, **751**, 51

Jones T., Ellis R. S., Richard J., Jullo E., 2013, *ApJ*, **765**, 48

Jones T., Stark D. P., Ellis R. S., 2018, *ApJ*, **863**, 191

Kewley L. J., Nicholls D. C., Sutherland R., Rigby J. R., Acharya A., Dopita M. A., Bayliss M. B., 2019, *ApJ*, **880**, 16

Kim J.-h., et al., 2018, *MNRAS*, **474**, 4232

Koester B. P., Gladders M. D., Hennawi J. F., Sharon K., Wuyts E., Rigby J. R., Bayliss M. B., Dahle H., 2010, *ApJ*, **723**, L73

Kubo J. M., et al., 2010, *ApJ*, **724**, L137

Labbé I., et al., 2013, *ApJ*, **777**, L19

Laporte N., Nakajima K., Ellis R. S., Zitrin A., Stark D. P., Mainali R., Roberts-Borsani G. W., 2017, *ApJ*, **851**, 40

Leethochawalit N., Jones T. A., Ellis R. S., Stark D. P., Richard J., Zitrin A., Auger M., 2016, *ApJ*, **820**, 84

Leitherer C., Tremonti C. A., Heckman T. M., Calzetti D., 2011, *AJ*, **141**, 37

Livermore R. C., Finkelstein S. L., Lotz J. M., 2017, *ApJ*, **835**, 113

Llerena M., et al., 2021, arXiv e-prints, [p. arXiv:2107.00660](https://arxiv.org/abs/2107.00660)

Luridiana V., Morisset C., Shaw R. A., 2015, *A&A*, **573**, A42

Mainali R., Kollmeier J. A., Stark D. P., Simcoe R. A., Walth G., Newman A. B., Miller D. R., 2017, *ApJ*, **836**, L14

Mainali R., et al., 2018, *MNRAS*, **479**, 1180

Mainali R., et al., 2020, *MNRAS*, **494**, 719

Mainali R., et al., 2022, *ApJ*, **940**, 160

Martin C. L., 2005, *ApJ*, **621**, 227

Maseda M. V., et al., 2017, preprint, ([arXiv:1710.06432](https://arxiv.org/abs/1710.06432))

McLean I. S., et al., 2012, in Society of Photo-Optical Instrumentation Engineers (SPIE) Conference Series, [doi:10.1111/12.924794](https://doi.org/10.1111/12.924794)

McLure R. J., et al., 2013, *MNRAS*, **432**, 2696

Nakajima K., et al., 2018, *A&A*, **612**, A94

Osterbrock D. E., Ferland G. J., 2006, Astrophysics of gaseous nebulae and active galactic nuclei

Parsa S., Dunlop J. S., McLure R. J., Mortlock A., 2016, *MNRAS*, **456**, 3194

Peng C. Y., Ho L. C., Impey C. D., Rix H.-W., 2002, *AJ*, **124**, 266

Pettini M., Steidel C. C., Adelberger K. L., Dickinson M., Giavalisco M., 2000, *ApJ*, **528**, 96

Pogge R. W., et al., 2010, in Ground-based and Airborne Instrumentation for Astronomy III, p. 77350A, [doi:10.1111/12.857215](https://doi.org/10.1111/12.857215)

Quider A. M., Pettini M., Shapley A. E., Steidel C. C., 2009, *MNRAS*, **398**, 1263

Ravindranath S., Monroe T., Jaskot A., Ferguson H. C., Tumlinson J., 2020, *ApJ*, **896**, 170

Reddy N. A., Steidel C. C., 2009, *ApJ*, **692**, 778

Rigby J. R., Rieke G. H., 2004, *ApJ*, **606**, 237

Rigby J. R., Bayliss M. B., Gladders M. D., Sharon K., Wuyts E., Dahle H., Johnson T., Peña-Guerrero M., 2015, *ApJ*, **814**, L6

Rigby J. R., et al., 2021, *ApJ*, **908**, 154

Roberts-Borsani G. W., et al., 2015, preprint, ([arXiv:1506.00854](https://arxiv.org/abs/1506.00854))

Robertson B. E., Ellis R. S., Dunlop J. S., McLure R. J., Stark D. P., 2010, *Nature*, **468**, 49

Rogers A. B., McLure R. J., Dunlop J. S., 2013, *MNRAS*, **429**, 2456

Saldana-Lopez A., et al., 2022, *A&A*, **663**, A59

Salmon B., et al., 2015, *ApJ*, **799**, 183

Sanders R. L., et al., 2016a, *ApJ*, **816**, 23

Sanders R. L., et al., 2016b, *ApJ*, **825**, L23

Sanders R. L., et al., 2020, *MNRAS*, **491**, 1427

Schaerer D., Izotov Y. I., Nakajima K., Worseck G., Chisholm J., Verhamme A., Thuan T. X., de Barros S., 2018, *A&A*, **616**, L14

Schaerer D., et al., 2022, *A&A*, **658**, L11

Schmidt K. B., et al., 2021, *A&A*, **654**, A80

Seive T., Chisholm J., Leclercq F., Zeimann G., 2022, *MNRAS*, **515**, 5556

Senchyna P., et al., 2017, *MNRAS*, **472**, 2608

Senchyna P., Stark D. P., Chevallard J., Charlot S., Jones T., Vidal-García A., 2019, *MNRAS*, **488**, 3492

Shapley A. E., Steidel C. C., Pettini M., Adelberger K. L., 2003, *ApJ*, **588**, 65

Sheinis A. I., Bolte M., Epps H. W., Kibrick R. I., Miller J. S., Radovan M. V., Bigelow B. C., Sutin B. M., 2002, *PASP*, **114**, 851

Silich S., Tenorio-Tagle G., 2017, *MNRAS*, **465**, 1375

Silich S., Tenorio-Tagle G., Muñoz-Tuñón C., 2007, *ApJ*, **669**, 952

Simcoe R. A., et al., 2008, in Ground-based and Airborne Instrumentation for Astronomy II, p. 70140U, [doi:10.1111/12.790414](https://doi.org/10.1111/12.790414)

Smit R., et al., 2014, *ApJ*, **784**, 58

Smit R., et al., 2015, *ApJ*, **801**, 122

Stark D. P., 2016, *ARA&A*, **54**, 761

Stark D. P., et al., 2013a, *MNRAS*, **436**, 1040

Stark D. P., Schenker M. A., Ellis R., Robertson B., McLure R., Dunlop J., 2013b, *ApJ*, **763**, 129

Stark D. P., et al., 2014, *MNRAS*, **445**, 3200

Stark D. P., et al., 2015a, Submitted to MNRAS, arxiv:1504.06881,

Stark D. P., et al., 2015b, *MNRAS*, **450**, 1846

Stark D. P., et al., 2017, *MNRAS*, **464**, 469

Steidel C. C., Erb D. K., Shapley A. E., Pettini M., Reddy N., Bogosavljević M., Rudie G. C., Rakic O., 2010, *ApJ*, **717**, 289

Steidel C. C., et al., 2014, *ApJ*, **795**, 165

Steidel C. C., Strom A. L., Pettini M., Rudie G. C., Reddy N. A., Trainor R. F., 2016, *ApJ*, **826**, 159

Strom A. L., Steidel C. C., Rudie G. C., Trainor R. F., Pettini M., Reddy N. A., 2016, preprint, ([arXiv:1608.02587](https://arxiv.org/abs/1608.02587))

Tang M., Stark D., Chevallard J., Charlot S., 2018, arXiv e-prints,

Tang M., Stark D. P., Chevallard J., Charlot S., Endsley R., Congiu E., 2021, *MNRAS*, **501**, 3238

Teplitz H. I., et al., 2000, *ApJ*, **533**, L65

Topping M. W., Shapley A. E., Stark D. P., Endsley R., Robertson B., Greene J. E., Furlanetto S. R., Tang M., 2021, *ApJ*, **917**, L36

Vanzella E., et al., 2016, *ApJ*, **821**, L27

Vanzella E., et al., 2017, preprint, ([arXiv:1703.02044](https://arxiv.org/abs/1703.02044))

Weiner B. J., et al., 2009, *ApJ*, **692**, 187

Whitmore B. C., et al., 2011, *ApJ*, **729**, 78

Xu X., et al., 2022, *ApJ*, **933**, 202

Xu X., et al., 2023, arXiv e-prints, p. arXiv:2301.04087

de Barros S., et al., 2016, *A&A*, **585**, A51

This paper has been typeset from a $\text{\TeX}/\text{\LaTeX}$ file prepared by the author.